International Journal of Extreme Manufacturing

TOPICAL REVIEW • OPEN ACCESS

Scalable metal-based nanoparticle synthesis via laser ablation in liquids for transformative sensory and synaptic devices

OPEN ACCESS
IMMT | IOP Publishing
International Journal of Extreme Manufacturing
Int. J. Extrem. Manuf. **7** (2025) 062001 (25pp)
https://doi.org/10.1088/2631-7990/ade836

Topical Review

Scalable metal-based nanoparticle synthesis via laser ablation in liquids for transformative sensory and synaptic devices

Jun-Gyu Choi[1], **Seokhyeon Baek**[2], **Junghoon Lee**[2,3,*] **and Sungjun Park**[1,2,*]

[1] Department of Electrical and Computer Engineering, Ajou University, Suwon 16499, Republic of Korea
[2] Department of Intelligence Semiconductor Engineering, Ajou University, Suwon 16499, Republic of Korea
[3] Material Technology Team, Common Technology Center, DS, Samsung Electronics, Hwaseong 18448, Republic of Korea

E-mail: jh8273.lee@samsung.com and sj0223park@ajou.ac.kr

Received 30 September 2024, revised 11 February 2025
Accepted for publication 25 June 2025
Published 7 July 2025

Abstract

Artificial sensory systems (ASS) are pivotal to next-generation extended reality technologies, now evolving into flexible platforms for comfortable wear and immersive user experiences, while ensuring high performance and operational reliability. To address these demands, metal-based nanoparticles (NPs), such as noble metal, oxide, and multi-elemental NPs, have been extensively incorporated into functional materials of sensory and synaptic devices due to their tunable optical, electrical, and chemical properties, enhancing sensory precision, stability, and environmental adaptability. However, traditional NP fabrication methods often involve complex processing, residual contaminants, and scalability issues, limiting their effectiveness in ASS applications. State-of-the-art laser ablation in liquids (LAL) presents a promising alternative, offering scalable production of surfactant-free NPs with customizable physicochemical properties, though their application in electronics remains underexplored. This review delves into the transformative potential of LAL-fabricated NPs in ASS, covering the fundamental mechanisms of LAL, the role of process parameters, the derivative strategies for size modulation, the diversity of metal-based NPs, their applications in sensory and synaptic devices, and the challenges and perspectives for meeting industrial standards. Bridging the

* Authors to whom any correspondence should be addressed.

gap between LAL and ASS is poised to revolutionize both industrial manufacturing and academic research by offering scalable solutions to overcome intrinsic tradeoffs between flexibility and performance, fostering innovations in human-centric, immersive electronics.

Keywords: laser ablation in liquids, nanoparticles, artificial perceptual sensors, synaptic devices

1. Introduction

Artificial sensory system (ASS), which mimics the intricate sensory networks of humans, is expected to play a critical role in the metaverse that offers immersive and interactive experiences for users with minimal spatial constraints through extended reality (XR) technology[1−5]. Initially developed for prosthetic applications and sensory augmentation[6,7], ASS has advanced with the integration of neural interfaces, enabling more precise replication of human perception, as demonstrated by commercially available technologies such as BrainPort and cochlear implants[8−11]. The emergence of electronic noses[12−14] and tongues[15−17] has further expanded their functional scope, showcasing real-world applications in healthcare and food quality assessment. Meanwhile, artificial intelligence-driven neural architectures have accelerated the development of artificial skin[18,19] and haptic interfaces[20,21], as exemplified by HaptX, Dexmo, and VRgluv, which enhance tactile feedback in virtual environments. The convergence of these technologies with high-resolution and spatially aware XR devices, such as Apple Vision, is further bridging the gap between digital and physical experiences. Despite significant progress in research and technological advancements, current wearable products are typically mounted on the head, hands, or other body parts, limiting user comfort and long-term wearability due to their bulky and heavy design. While strategies to improve flexibility have shown promise, they often introduce tradeoffs in performance degradations, such as reduced sensing fidelity or mechanical durability. Additionally, their high production costs remain a major obstacle to widespread adoption, necessitating innovative material strategies that can enhance functionality without compromising flexibility, durability, and cost-efficient scalability.

Nanoparticle (NP) incorporation into ASS has emerged as a promising approach to overcoming these limitations, leveraging the unique physicochemical properties of nanomaterials to enhance sensory precision, stability, and functionality[22−24]. These involve tunable optical properties, robust chemical stability, and diverse functionalities, enabling efficient signal transduction, improved environmental resilience, and dynamic adaptation in ASS architectures[25−27]. Furthermore, their high surface-to-volume ratio facilitates stronger interactions with biological or external stimuli, significantly improving detection sensitivity and response time—both critical for real-time and high-fidelity sensory applications.

Given the considerable advantages of NPs to ASS, numerous synthesis techniques have been explored, including chemical/physical vapor deposition[28−30], sol-gel processing[31−33], hydrothermal synthesis[34−37], and electrochemical deposition[38−40]. Achieving high-purity NPs is critical for tailoring desired properties and preventing device performance degradation. Physical deposition methods, such as vacuum-based techniques, ensure high-purity NPs but are unsuitable for mass production due to their complex processing requirements and high energy consumption. On the other hand, liquid-phase techniques, known for their high production efficiency, are often applied ex-situ and require surfactants or ligand chemistry to prevent aggregation and maintain colloidal stability[41,42]. These organic residues introduce unwanted electrical barriers or interfere with device performance, which should be eliminated. These limitations necessitate alternative synthesis strategies that can deliver high production efficiency while maintaining optimal electronic and structural integrity.

As an alternative, the laser ablation in liquid (LAL) technique promises solutions to address many of the limitations inherent to conventional NP synthesis methods. By using a focused laser to ablate a solid target immersed in a liquid, LAL generates NPs through laser-induced plasma and rapid cooling, with their adjustable physicochemical characteristics by controlling the fabrication parameters[43−45]. While LAL historically suffered from relatively lower productivity than other synthesis techniques, recent advancements have significantly improved its scalability, achieving production efficiencies over 8 $g{\cdot}h^{-1}$[46,47]. Beyond productivity improvements, LAL offers distinctive advantages that position it as an optimal solution for wearable and flexible ASS applications. Unlike vacuum-based deposition methods, LAL-generated NPs can be directly integrated into the synthesis step of functional materials, eliminating reliance on multi-step chemical processing. This simplifies fabrication while reducing the risk of performance degradation due to residual contaminants. Moreover, considering the versatile functionalities of alloy NPs, LAL offers a relatively easy route to achieve various alloy structures with precise composition controls. However, a significant portion of LAL-based NP synthesis research has still focused on their applications in catalysis and drug delivery rather than ASS[48−50]. This indicates a gap in fully realizing its potential for sensory and synaptic devices, where its ligand-free nature, high purity, and process scalability could offer transformative benefits. Expanding the scope of LAL toward ASS applications could drive innovation in immersive

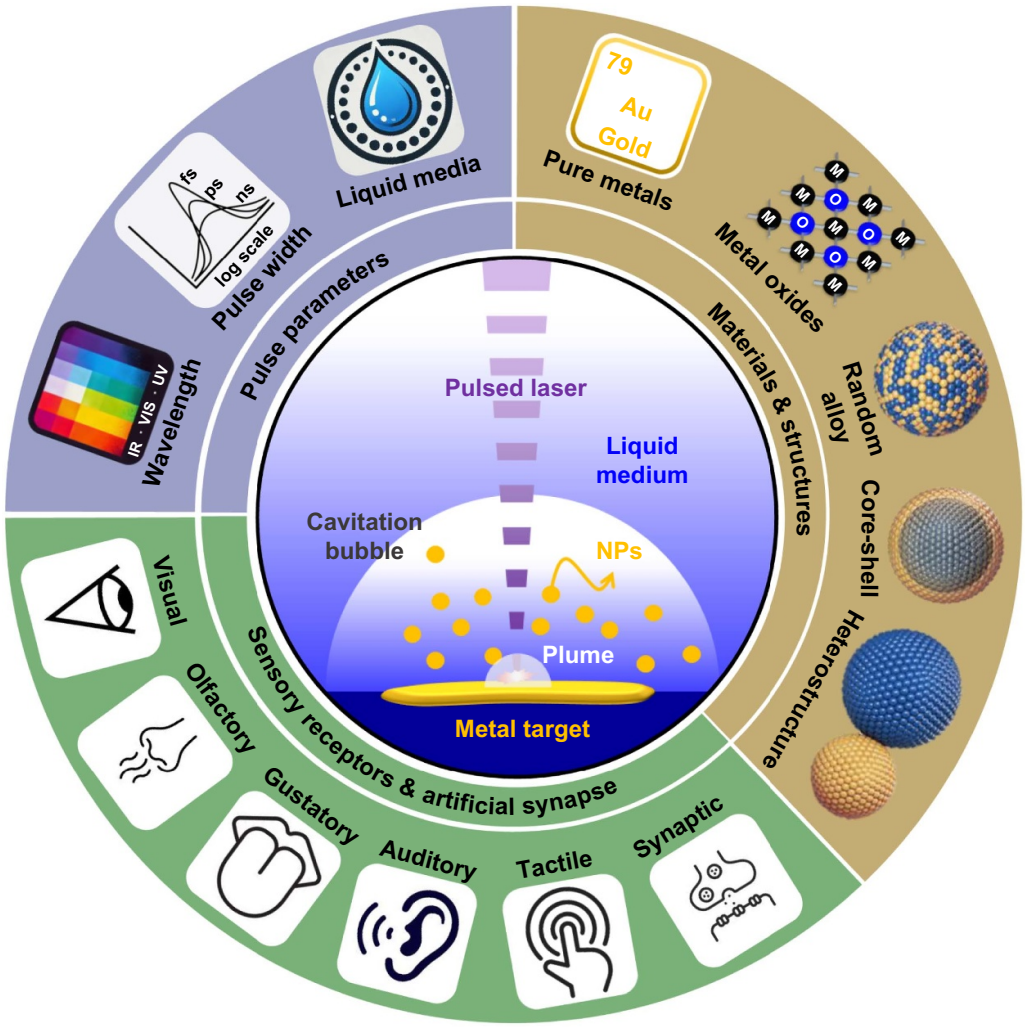

Figure 1. Schematics of the laser ablation in liquid (LAL) process for scalable nanoparticle (NP) fabrication, highlighting an overview of this review. Key aspects of this review: the process parameters determining NP features, metal target-derived materials and structures, and applications in various sensors and synaptic devices.

technologies, bridging the gap between material synthesis and next-generation ASS platforms.

This review explores the transformative potential of LAL-fabricated NPs in ASS, emphasizing their role in advancing high-performance sensory and synaptic devices. Figure 1 outlines the scope of review, which includes the working mechanism of LAL, key parameters influencing the characteristics of NPs, and advancements in achieving advanced NP structures. Subsequently, the review explores various applications of NPs in enhancing sensory (visual, olfactory, gustatory, auditory, tactile sensors) and synaptic devices, emphasizing the transformative potential of LAL-fabricated NPs in expanding high-performance device capabilities and fostering innovation in immersive technologies. By providing a comprehensive analysis of both foundational principles and cutting-edge developments, this review aims to chart a path for future research and technological breakthroughs, underscoring the pivotal role of LAL-fabricated NPs in revolutionizing ASS and advancing the frontiers of electronics.

2. Advancement in LAL for ASS

Nanoparticles (NPs) have been used in a wide range of fields, involving electrochemistry, optics, and electronics. Among them, metal-based NPs, such as mono-/bi-atomic[51–55], metal oxide NPs[56–58], and high-entropy alloys (HEAs)[59–63], are gaining attention due to their unique and versatile functionalities. Particularly for sensory and synaptic devices, they commonly demonstrate surfactant-free synthesis, high surface-area-to-volume ratio, and tunable physicochemical properties, all of which are crucial for enhancing device performance. In sensor devices, NPs need to be highly conductive and reactive to quickly detect and convert external signals into electrical outputs. On the other hand, synaptic devices require NPs that can store and control charges, supporting learning and memory-like functions. These differences necessitate specific synthesis strategies tailored to each application, highlighting the role of LAL in enabling customizable NP properties through precise parameter adjustments

while maintaining a surfactant-free nature. This chapter integrates insights from the fundamental understanding of the LAL process, techniques for overcoming productivity limitations, and advancements in LAL-based NP engineering. By bridging these aspects, it provides a comprehensive framework for tailoring NP synthesis to meet the demands of ASS applications.

2.1. Fundamental mechanisms of LAL

LAL is a technique where high-energy laser pulses are directed at a solid target immersed in a liquid medium, resulting in the formation of plasma and subsequent NP generation through rapid cooling and nucleation[64,65]. Since vacuum equipment is not required, the LAL setup is relatively affordable and streamlined[66], primarily consisting of a laser source, focusing lens, and liquid vessel containing the metal target. Figure 2(a) presents the schematic setup for LAL, featuring controllable pulse parameters such as wavelength, pulse width, and repetition rate. The infinite combination of pulse parameters and liquid media allows for flexible modulation of the physicochemical properties of the resulting NPs, including their composition, structure, and size[67]. Figure 2(b) shows a snapshot of a LAL-triggered suspension of colloidal NPs in deionized (DI) water, produced from a 5 mm Au plate.

Spectroscopic and microscopic analyses indicate that the fundamental mechanism of LAL involves a specific sequence of events (Figure 2(c)). Shadowgraphs, alongside high-speed cameras, provide detailed insights into the key stages of LAL, including plasma formation, bubble dynamics, and nanoparticle generation, making them essential for optimizing the process for scalable NP production. The LAL process commonly involves four phases: laser-matter interaction, plasma formation, cavitation bubble dynamics, and NP formation[55,70−72]. Understanding each stage comprehensively is crucial for optimizing the process for scalable NP production. The process begins with the interaction of a laser beam with a liquid-immersed solid target. The high-intensity laser pulse causes rapid heating and phase transition at the target–liquid interface, forming plasma with ultrahigh pressure and temperature. Despite energy loss during laser propagation, the laser pulse reaching the target surface converts the solid target into the plasma phase. Pulses with femtosecond-scale duration preferentially led to the oscillation of electrons in the target lattice owing to a short lifetime, resulting in the release of heat. Consequently, a phase transition in the solid target results in the dissociation of atomic bonds. In contrast, pulses with relatively long durations induce sufficient heating to vaporize the target by Coulombic mechanisms, leading to plasma formation. While the fundamental mechanisms of laser-induced plasma formation in liquid environments share similarities with those in gaseous or vacuum environments, the liquid medium plays a unique role in rapid quenching and minimizing impurities[73]. This distinct environment promotes the controlled nucleation and growth of high-purity NPs, setting LAL apart from other ablation techniques. After initial laser-matter interaction, a plasma plume comprising a dense mixture of ionized and atomized species is formed. Laser-matter interactions permit rapid plume expansion owing to the high pressure in the cavitation bubbles, generating shockwaves that propagate through the surrounding liquid. Instantaneous quenching leads to bubble shrinkage, and the adiabatic closed system releases extremely high temperatures. Plasma species undergo nucleation and growth under repetitive bubble rebounds, which significantly influence the morphology, crystallinity, and size distribution of the resultant NPs.

2.2. Role of process parameters

Understanding the role of LAL parameters, including pulse parameters (i.e., the wavelength, pulse duration, fluence, and repetition rate) and design factors (i.e., the liquid media, vessel architecture, and multiple lasers), is important for ensuring the consistent high productivity of NPs through the LAL process. Intertwined parameters make accurate predictions and analyses challenging, permitting only inductive approaches through multiple experiments. This section discusses the generally accepted role of a specific parameter, excluding its interactions with all other parameters. The fluence, which indicates the energy of the laser source per unit area and directly affects the ablation rate and NP yield, is a critical LAL parameter. Figure 2(d) shows schematics of fluence-dependent ablation. The ablation rate of LAL shows a logarithmic relationship with fluence, indicating enhanced productivity with increasing fluence[74−76]. Moreover, determining the threshold fluence is crucial for optimizing production efficiency and power consumption, both of which are important parameters for industrial application. The threshold fluence, representing the minimal fluence for ablation, is predominantly influenced by the thermodynamics and optical properties of individual materials, such as absorbance and surface reflectivity; efficiency reductions beyond this threshold are attributed to shielding effects of the ducts and bubbles[72,77]. A higher fluence generally promotes smaller NPs through increased fragmentation caused by elevated thermal energy[74]. However, NP size is also influenced by complex factors, including plasma dynamics, target material properties, and bubble shielding effects. Therefore, achieving optimal fluence requires precise modulation tailored to specific materials for maximal NP yield and size uniformity.

The laser wavelength significantly influences the NP shape, size, and colloidal density, which can be calculated from the weight of the ducts per unit volume. Typically, shorter wavelengths (UV or visible) with high-absorption cross-sections result in smaller NPs and higher colloidal densities than longer wavelengths (IR) owing to efficient energy transfer to the target material[78]. However, shielding effects by concentrated particles (Rayleigh scattering) and/or permanent bubbles are observed in systems with relatively short wavelengths and high-absorption cross-sections, resulting in a lowering of the ablation rate and productivity[79]. Figure 2(e) shows schematics of the wavelength-dependent ablation efficiency based on the initial cycle of the LAL assuming an infrequent repetition of the process. However,

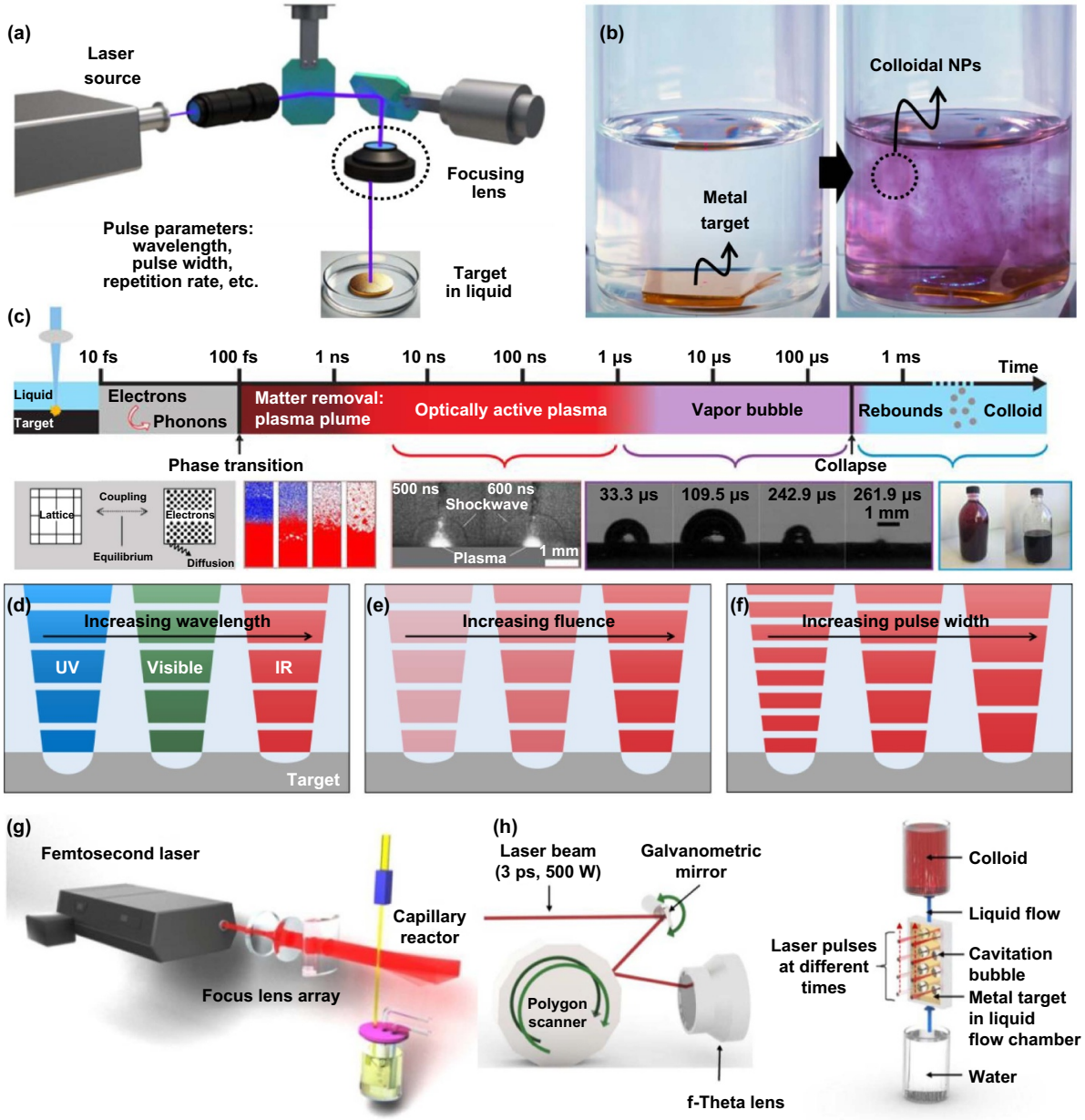

Figure 2. Fundamentals of the LAL process and the role of the process parameters. (a) Schematics of LAL equipment with the target submerged in a liquid bath. (b) Photographs showing NP production by the LAL process. (c) Time-sequential progress of the LAL process (from light-matter interaction to colloidal NP formation). Reproduced from[27]. CC BY 4.0. Schematics of the key parameters determining the productivity of the LAL process: the (d) wavelength, (e) fluence, and (f) pulse width. Advanced LAL technologies to enhance production rates; (g) continuous flow system of target-containing liquid. Reprinted from[68], © 2017 Published by Elsevier B.V. (h) Laser-steering systems with a polygon scanner. Reproduced from[69]. © IOP Publishing Ltd. All rights reserved.

in practical applications involving repetitive LAL cycles, the optical properties, such as absorbance, evolve due to cumulative effects such as surface ablation, melting, and the ablation of previously generated NPs. These changes influence energy absorption, making it essential to experimentally determine the optimal wavelength through iterative testing and adjustments.

The pulse width or duration significantly influences the ablation mechanism, productivity, and features of NPs produced by the LAL process. In particular, plasma dynamics depend on the laser pulse width. The ablation mechanism for shorter widths is based on Coulomb explosions with electron-phonon coupling. As the derived electron excitation occurs prior to significant heat diffusion, shorter pulse widths yield higher productivity and smaller NPs by minimizing thermal diffusion and favoring a non-thermal ablation mechanism (Figure 2(f)). In contrast, during the sequential processes that occur with longer pulse widths, including material melting and cavitation bubble formation, the solid target remains irradiated by the laser beam, leading to thermal loss and low productivity.

Therefore, the pulse-material interaction varies significantly with the pulse duration, influencing the ablation mechanism and, consequently, the characteristics of the resultant NPs.

The liquid medium and its properties, such as viscosity, transparency, and chemical compositions, significantly influence the LAL process. To ensure effective energy transfer, the liquid must be transparent to the laser wavelength used in the LAL process. High-viscosity liquids can hinder the dissipation of gas bubbles, leading to persistent bubbles that scatter or reflect subsequent laser pulses, ultimately reducing productivity[44]. Persistent microbubbles in viscous liquids like ethylene glycol can limit productivity by shielding the laser beam, while low-viscosity solvents allow efficient bubble transport and minimize such losses[80]. The transparency of the liquid to the laser wavelength also plays a pivotal role in ensuring effective energy transfer. The chemical composition of the liquid governs NP size, crystallinity, and stability, primarily by inducing specific surface interactions or decomposition pathways. Organic solvents, such as acetone and alcohol, promote diverse decomposition reactions, leading to enhanced hydrogen gas formation and stabilization of colloids. This is attributed to the fact that the organic solvents with higher carbon chain lengths tend to generate smaller NPs and exhibit higher productivity[81,82]. Furthermore, dissolved gases and reactive species in the liquid significantly impact NP composition. In aqueous systems, water splitting leads to oxidation, influencing the formation of oxide shells or phases. In contrast, organic solvents provide an inert environment, suppressing oxidation and enabling the formation of pure metallic or core–shell nanoparticles with enhanced surface stability[83,84]. Ultimately, optimizing liquid properties is crucial for balancing productivity, particle quality, and functional surface coatings, offering tailored routes for scalable NP synthesis.

Regarding productivity, Barcikowski's group reported that laser-based synthesis of colloidal metal NPs, specifically the highly prestigious Au NPs, became more economical than chemical reduction when the NP productivity exceeded 550 $mg{\cdot}h^{-1}$[85]. Although this transition highlights the potential of LAL in achieving large-scale and cost-effective NP production, meeting the break-even for industrialization, they have still suffered from relatively low productivity with milligrams to gram per hour, depending on the setup and conditions, compared to other processes. For example, wet chemical synthesis methods typically achieve production rates over several tens of grams per day[86–88], while those using flame spray pyrolysis[89,90] and arc discharge[91] reach several kilograms per hour. A sufficient processing time with a high repetition rate was attempted for efficient LAL, but extended ablation with excessive repetition led to an underestimation of productivity due to variations in target roughness, persistent bubbles, and particle-induced laser shielding[92]. Ensuring that each pulse interacts with a fresh target surface and liquid environment is crucial for maintaining consistency and quality. The working distance of the laser beam determines the spot size and is focused on the area of the ablated target. Besides resulting in higher energy densities and more efficient ablation, smaller spot sizes may increase the risk of self-absorption and scattering effects. Optimizing the working distance between the target and focusing lens can balance the energy density and ablation efficiency. To address these limitations, advanced laser technology and strategic designs have been proposed. Figures 2(g) and (h) present continuous flow-jet designs for target-containing liquid[68,93–95] and laser-steering technologies with various scanners[69,96,97], respectively, facilitating a higher throughput and consistent NP characteristics. While these strategical designs significantly enhance production efficiency, the lack of their long-term storage without using surfactant remains an obstacle for industrial production, necessitating future studies on overcoming the tradeoff between productivity and stability. Additionally, understanding the complex interplay among intertwined process parameters is desired for optimizing the LAL process. Studying these interactions will help guide future research by offering insights into achieving optimized physicochemical properties, enhanced device performance, and scalable NP production.

2.3. LAL-derived size modulation

Although most previous studies focused on LAL with certain solid targets, LAL with dispersed NPs is a promising strategy for generating NPs with varied size distributions (Figure 3(a)). In contrast to the infrequent LAL, the repeated LAL indicates the secondary and/or subsequent ablation of dispersed NPs in liquid media. Figure 3(b) shows the LAL-derivative processes (laser fragmentation in liquid (LFL) for downsizing and laser melting in liquid (LML) for upsizing) used for rearranging the sizes of colloidal NPs. The flexibility and efficacy of the techniques in controlling the size and properties of NPs make them valuable for applications in catalysis, medicine, and materials science. Furthermore, lots of investigations have empirically demonstrated effective results in achieving precise size modulation, for both LFL and LML, whereas infrequent LAL without repetition often faced limitations in this area.

LFL, which typically generates NPs that are several tens of nanometers in size, is strategically effective in enhancing NP productivity. LFL uses ligand-free NPs as target source with stabilizing molecules or other supports such as metal oxides. Pulses with a relatively short wavelength and high fluence facilitate LFL prior to NP agglomeration[99,101]. The fragmentation efficiency can be assessed through the mass-specific energy input, which represents the total energy applied to the particle mass; this input, which is controlled by the number of pulses per liquid volume element and flow rate, enables precise control of the particle size and properties. A recent study by Nyabadza et al. reported the liquid-dependent size distribution of Mg NPs synthesized by LAL[102]. The mean sizes of Mg NPs synthesized in IPA and DI water were 52 nm and 89 nm, respectively, highlighting that LAL in organic solvent is much more effective for LFL rather than oxidizing solvent like DI water. A study by Ziefuß et al. demonstrated the synergistic effects between specific halide anions and pH, which were found to significantly influence the particle size distribution by LFL, particularly in the production of ligand-free

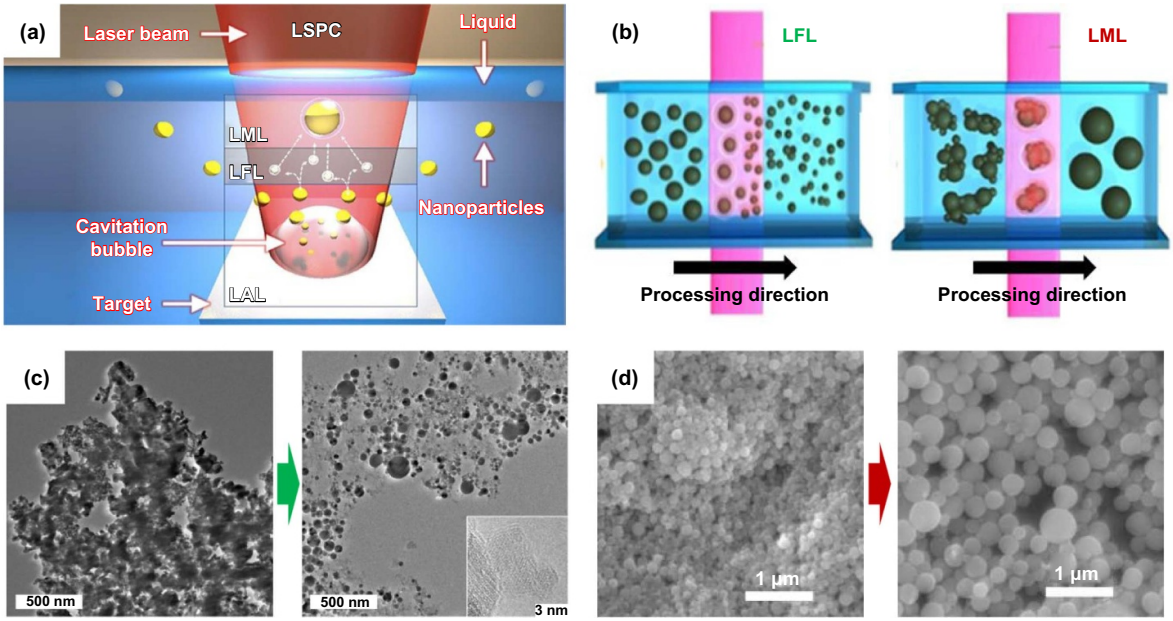

Figure 3. Strategies for engineering LAL-derived NPs with different sizes. (a) Conceptual schematics of the laser fragment in liquid (LFL) and laser melting in liquid (LML) processes during LAL with a solid metal target. Reprinted with permission from[98]. Copyright (2017) American Chemical Society. Schematics of the (b) LFL and LML processes in the absence of a specific solid target for tailoring the size of dispersed NPs. Reproduced from[27]. CC BY 4.0. (c) High-resolution transmission electron microscopy (HR–TEM) images of $CoFe_2O_4$ NPs with the relative volume, surface, and diameter distributions before and after LFL. Reproduced from[99]. CC BY 4.0. (d) Scanning electron microscopy (SEM) images of Ge NPs with the size distribution before and after LML. Reproduced from[100]. CC BY 4.0.

Au NCs[103]. They proved that the presence of chaotropic anions such as bromide and iodide led to a more pronounced size quenching effect, enhancing the yield of particles smaller than 3 nm in neutral pH conditions. Additionally, Figure 3(c) shows high-resolution transmission electron microscopy (HR–TEM) images of $CoFe_2O_4$ NPs with the relative distributions of volume, surface area, and diameter before and after LFL[99].

In contrast, LML utilizes the laser irradiation of a particulate material dispersed in a liquid to induce thermal processes, particularly melting, to fabricate new particles[104–108]. This can result in isochoric melting, particle reshaping, or an increase in particle size through fusion, without any chemical reagents. LML is particularly effective in creating single-crystalline microspheres from various materials, with the ability to precisely tailor particle size and surface structure by adjusting the input laser fluence that is typically one to two orders of magnitude lower than conventional LAL[109]. During LML, the laser beam heats particles, causing them to form transient molten droplets, which are subsequently quenched by the surrounding liquid to form spherical solid particles. This process can yield sub-micrometer spherical particles, often in the 100–200 nm size range. However, adequate fluence control is vital for sub-micrometer particle synthesis without inducing vaporization. The size–fluence relationship can be visualized using size-fluence diagrams, which help predict the particle sizes obtained under different conditions. Studies investigating the dispersed TiO_2 particles irradiated at various fluences using the third harmonic (355 nm) of a Nd:YAG laser confirm the effect of fluence on the particle size and the formation of sub-micrometer particles through LML[110,111]. A study by Song et al. demonstrated that LML could induce morphology evolution and phase transformation in Fe_2O_3 NPs, leading to the formation of well-defined sub-micrometer spheres[112]. The transformation was finely controlled by adjusting laser fluence and irradiation time, highlighting the precision of LML in tailoring properties of NPs. Additionally, Figure 3(d) shows scanning electron microscopy (SEM) images of Ge NPs with the size distributions before and after LML[100].

2.4. LAL for multi-elemental NPs

The functionality of NPs can be significantly broadened by integrating them with other metals or materials, leading to the formation of binary alloys, core–shell structures, or heterostructures (Figure 4(a)). These binary nanoparticles (BNPs) exhibit diverse characteristics depending on their composition and structural configuration, with LAL offering a versatile method to generate them using two metallic targets or sources. Binary alloy NPs emerge when two metals are uniformly mixed at the atomic level to form a single-phase solid solution. Their physicochemical and optical properties can be finely tuned by adjusting the metal composition ratios. For example, increasing the proportion of Ag in Au–Ag alloy NPs results in relatively small and spherical NPs owing to differences in ablation efficiencies and atomic diffusion rates[113]. The optical properties of a system, particularly surface plasmon resonance (SPR), can be precisely tuned by metal composition modulation. Gradually varying the Ag

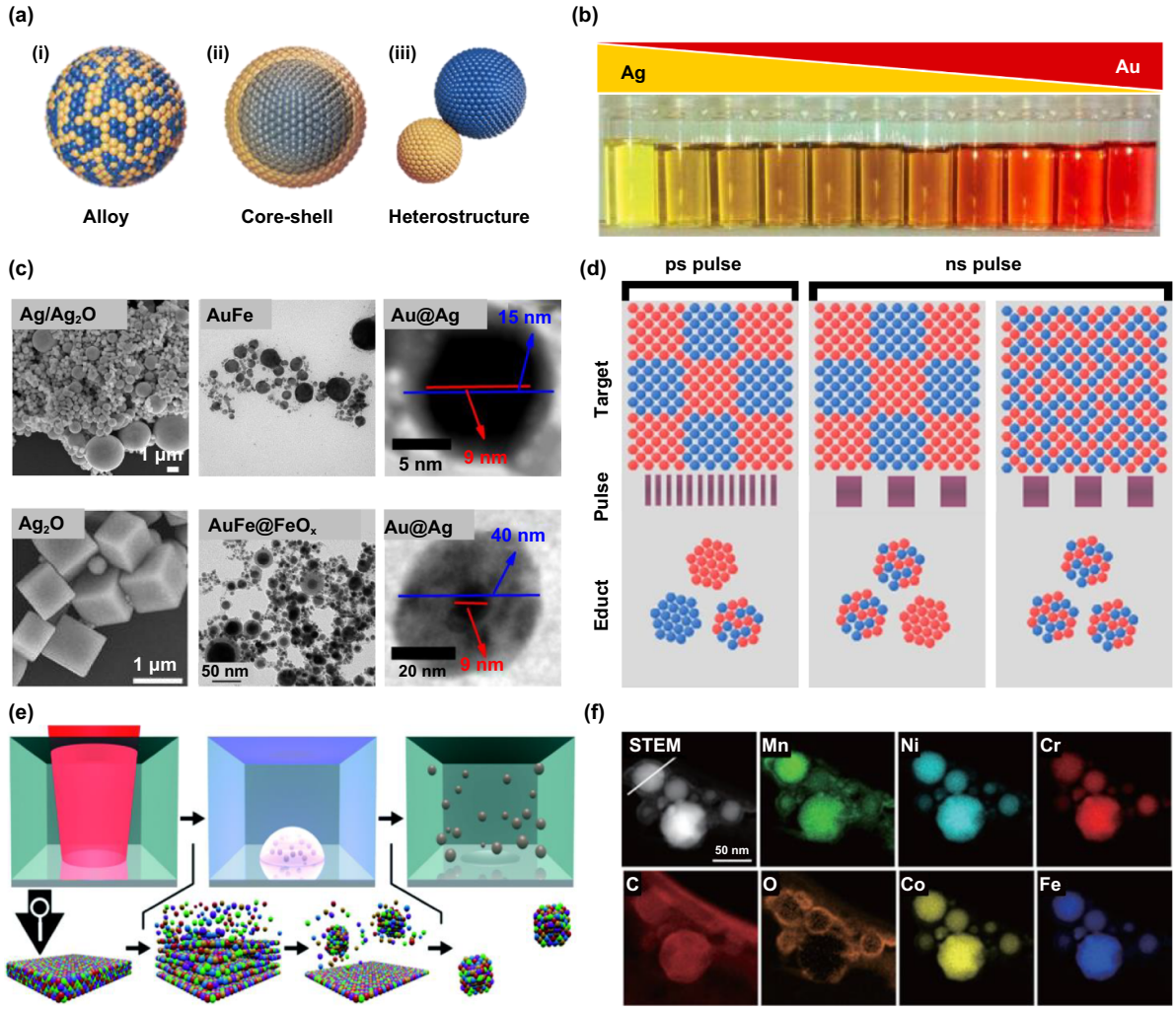

Figure 4. LAL for producing various multi-elemental NPs. (a) Schematics of the following types of binary nanoparticles (BNPs): (i) random alloy, (ii) core-shell structure, and (iii) heterostructure. (b) Photographs of Ag–Au colloidal NP solutions containing different Ag: Au molar ratios leveraged by the composition of Ag and Au NPs. Reproduced from[113] with permission from the Royal Society of Chemistry. (c) Microscopic images of NPs synthesized from identical target materials under distinct oxidative conditions by leveraging pulse parameters and the liquid medium. Ag/Ag_2O and Ag_2O systems: Reprinted with permission from[118]. Copyright (2011) American Chemical Society. AuFe and $AuFe@FeO_x$ systems: Reprinted from[119], © 2016 Elsevier Inc. All rights reserved. Au@Ag systems: Reproduced from[120]. CC BY 4.0. (d) Schematics of resultant NPs depending on pulse duration and order of mixed metal targets, respectively. Reproduced from[52]. CC BY 4.0. (e) Schematics of sequential LAL process for synthesizing bulk high-entropy alloy NPs. Reproduced from[121] with permission from the Royal Society of Chemistry. (f) High-angle annular dark-field (HAADF) scanning transmission electron microscopy (STEM) image and energy dispersive X-ray (EDX) elemental maps of LAL-derived $Cr_{17.5}Co_{17.5}Fe_{17.5}Ni_{17.5}Mn_{30}$ NPs. Reproduced from[122]. CC BY 4.0.

to Au molar ratio in alloy NPs shifts the SPR peak associated with the system, resulting in colloid solutions with different colors (Figure 4(b)). This tunability expedites biosensing and imaging applications, which require specific wavelengths for optimal performance. The ability to control optical properties through composition permits the design of NPs with tailored absorption and scattering characteristics with high efficacy in optical applications. On the other hand, NPs with a core–shell structure feature a core material encapsulated by a shell, each comprising different substances with complementary functions. The shell typically provides stability, prevents oxidation, and can introduce surface functionality such as biocompatibility or chemical resistance, while the core contributes key optical, electronic, or catalytic properties. For instance, in $Ag@WO_3$ core–shell NPs synthesized via LAL, the Ag core was responsible for generating strong localized surface plasmons, enhancing light-matter interactions and electrical conductivity[114]. Meanwhile, the WO_3 shell imparted gas-sensing capabilities and optoelectronic properties due to its semiconductor nature and tunable bandgap. Heterostructures for binary NPs consist of two distinct materials that form separate, identifiable domains within a single NP, creating interfaces that enable synergistic interactions and unique properties. For example, Au/TiO_2 heterostructure NPs exhibited strong catalytic activity, benefiting from efficient charge transfer at their interface, which reduced electron-hole

recombination and enhanced CO oxidation performance[115]. Similarly, Au/Fe_xO_y heterostructures combined the plasmonic optical properties of Au with the magnetic properties of Fe_xO_y, making them suitable for bifunctional applications. To produce these BNPs, two LAL processes are generally employed: sequential and reactive LAL (S- and R-LAL, respectively). S-LAL, which involves the sequential ablation of different metal targets in the same liquid solution, enables the fabrication of core-shell or alloy BNPs through ablation-step (order and duration) control. D'Urso et al. reported the sequential ablation of Zn and Au in the same batch to produce ZnO–Au heterostructures[116]. The shell thickness and alloy composition of the resultant NPs are determined by the ablation-step sequence and relative ablation times. R-LAL, which involves the ablation of a metal target in a solution containing reactive species or precursors from another metal, facilitates the in-situ formation of complex nanostructures. The ablation of Cu in a solution containing Pt salts, for instance, results in Pt–Cu alloys or core-shell structures comprising a Cu core and Pt shell[117]. The reactive species in the solution promote the formation of the desired structure during ablation, enabling the synthesis of complex BNPs with tailored properties through a single-step method.

Several LAL process parameters, including the pulse width, laser wavelength, and fluence, as well as the oxidative or reductive conditions of the surrounding liquid medium influence the characteristics of BNPs synthesized through LAL. Figure 4(c) shows microscopic images of various BNPs synthesized using the same target. The liquid medium is the primary parameter influencing the oxidative state of the resultant BNPs; the chemical environment during LAL (oxidative or reductive) significantly affects the oxidation state and composition of the resultant NPs. Ablation in oxidative environments, such as water- or air-saturated solutions, tends to produce metal oxides or higher oxidation states, whereas ablation in reductive environments, such as inert gases or reducing agents, favors the formation of pure metal NPs or lower oxidation states. In the LAL synthesis of Ag_2O NPs in DI water containing polysorbate 80 reported by Yan et al., the concentration of polysorbate 80 determined the oxidative state of the resultant NPs[118]; heterostructures comprising Ag spheres and Ag_2O were preferentially formed at low and high concentrations of polysorbate 80, respectively. A paper by Amendola et al. reported the effects of solvents on the structure of LAL-synthesized BNP[119]. LAL with a target comprising a layered thin film of Au and Fe in ethanol and DI water resulted in the formation of AuFe alloy and AuFe@FeO_x core-shell NPs, respectively. Low oxidation-state NPs can be synthesized in organic solvents such as isopropyl alcohol, ethanol, toluene, and tetrahydrofuran. A study by Wagener et al. reported LAL with a $Fe_{44}Au_{56}$ alloy target in diverse liquid media, including DI water, acetone, and methacrylate[84]. Only a small amount of alloy BNPs showed the composition ratio of the target; moreover, the BNPs synthesized in organic solvents and DI water exhibited Fe@Au and Au@Fe_3O_4 core–shell structures, respectively, owing to the different oxidation states of each metal.

In addition to solvent variations, the pulse parameters also influence the stoichiometry or characteristics of the BNPs produced by LAL. Relatively short wavelengths, such as UV light, produce small particles with a uniform size distribution (owing to high energy absorption and efficient fragmentation) and high probability of oxidation[123]. The pulse width also influences the phase and crystallinity of LAL-synthesized NPs. A study by Bonis et al. compared the educts generated by the LAL of a GaAs target immersed in acetone with ns- and fs-pulses[124]. While the ns-pulse LAL produced Ga_2O_3 with little GaAs due to melting-derived excess atomic Ga species, pure polycrystalline GaAs NPs were produced in fs-pulse LAL, possibly owing to the limited laser-material interaction time, which limited the possibility of significant melting and non-stoichiometric evaporation. Validating the effect of the laser fluence on NP fabrication through LAL, Altowyan et al. reported the fabrication of Au@Ag core-shell NPs with different shell thicknesses (within 6–31 nm) through ablation-energy variation (increasing the ablation energy while keeping the other parameters constant) in an R-LAL process[120]. Alloy-target variation is another useful strategy for modifying the structure or composition of LAL-synthesized BNPs. Figure 4(d) shows schematics of the effects of Co–Fe target sintering and pulse duration on the NPs produced through LAL. Waag et al. reported that the reliance on pulse width was weakened in sintered target, a randomly mixed structure[52]. The study concluded that the mixing of Co and Fe primarily occurred in laser-irradiated, heat-affected target regions rather than in the ablated plume, and that achieving better mixing might require reducing laser energy density or increasing the pulse duration.

Unlike typical alloy NPs, HEA NPs are defined by their multicomponent nature, incorporating five or more metallic elements at near-equiatomic ratios. Their unique high-entropy mixing states enable them to maintain a homogeneous solid-solution phase while suppressing phase separation, resulting in enhanced thermal stability, corrosion resistance, and mechanical robustness compared to binary or ternary alloys[60,61]. The configurational entropy gained by combining multiple elements provides diverse active sites and structural stability even under extreme conditions, making them ideal for applications in catalysis[125,126], sensing[59,63], and energy storage[127]. Among various synthetic approaches, LAL emerged recently as a reliable method for producing colloidal HEA NPs with controlled composition and high scalability[121]. Figure 4(e) presents the sequential process of LAL for producing HEA NPs. During these processes, a laser beam ablates the surface of an HEA target immersed in liquid, forming a plasma plume that cools rapidly, resulting in multi-elemental mixing and quenching into uniform NPs. Due to an ultrafast response, LAL ensures minimal phase separation and enables the synthesis of HEA NPs ranging from crystalline to amorphous structures[60]. Additionally, the liquid environment can be tailored to influence the oxidation state and surface chemistry of the resultant HEA-NPs, enhancing their functionality for targeted applications.

Similar to typical LAL-derived NPs, HEA NPs also demonstrate exceptional tunability in size, phase distribution, and composition, depending on the ablation parameters and liquid medium used. For instance, LAL, investigated by Waag et al., using alloy targets composed of Co, Ni, Fe, Cu, and Mn in an ethanol medium resulted in homogeneous HEA NPs with a face-centered cubic structure, offering high catalytic activity and stability in hydrogen evolution reactions[121]. Meanwhile, Johny et al. successfully demonstrated amorphous $Cr_{17.5}Co_{17.5}Fe_{17.5}Ni_{17.5}Mn_{30}$ NPs through LAL of respective bulk targets in acetonitrile, employed for bifunctional electrocatalysts[122]. Figure 4(f) displays the high-angle annular dark-field (HAADF) scanning transmission electron microscopy (STEM) image and energy dispersive X-ray (EDX) elemental maps of the corresponding HEA NPs. This amorphous state not only enhances surface active sites but also imparts superior corrosion resistance and durability during electrocatalytic reactions, making HEMG NPs ideal for oxygen evolution and reduction reactions. Furthermore, by tuning the laser fluence and liquid environment, the elemental composition, size distribution, and surface chemistry of HEA NPs can be precisely controlled, offering exceptional flexibility in tailoring electrocatalytic performance. Benchmarking this, extending HEA NPs beyond their well-established applications in electrochemistry and catalysis could unlock significant potential in sensory and synaptic devices, where their multicomponent nature, high surface area, and tunable electronic properties could enable enhanced sensitivity, multifunctional sensing, and dynamic memory functions critical for advanced ASS applications.

3. Scalable, ligand-free NPs for advanced ASS applications

With adequately defined process parameters, LAL enables the scalable, large-scale, cost-effective synthesis of NPs with a specific size, shape, composition, and structure. Versatile NPs exhibit high potential applicability in extensive fields. While limited amounts of NPs are required in certain fields of application, such as catalysis and medicine, the scalable production of NPs is a prerequisite for state-of-the-art electronics owing to rapid industrial expandability and the requirement of large-area processability. This section reviews the applicability of ligand-free NPs in human-like electronics, particularly mimicking five-sense receptors and synapses, which emphasize the transformative potential of LAL for advanced ASS.

3.1. NP applications in visual and olfactory sensors

The sensing mechanisms of the five human senses (i.e., the visual, olfactory, gustatory, auditory, and tactile senses) vary distinctly. However, in all the sensing mechanisms, receptors detect stimuli and convert them into electrical signals, transmitted to the brain through neural pathways[128]. Functional sensory devices that detect light, gas, chemicals, vibration, pressure, temperature, and humidity can function as artificial receptors in human-like sensory systems for extended reality applications.

The primary function of a photodetector is to convert light into electrical signals by processing visual information, which involves the colors, motion, depth, patterns, and shapes arising from the recognition of differences in light intensity leveraged by wavelength, time, and distance[129–132]. Array-type photodetectors with different absorption wavelengths can be used to detect the colors of the target[133,134]. According to a study by Montaño-Priede et al. that calculated the maximum absorption wavelengths of Au NP-dispersed solutions by changing the NP diameter, shape, and interparticle distance (Figure 5(a)), solutions with different sizes and shapes of Au NPs exhibited different colors[135]; subsequently, this study identified the optimal geometrical parameters for maximizing this color difference upon NP clustering. Additionally, Lee et al. reported solution-processed inorganic UV–visible short-wave-infrared photodetectors comprising highly monodispersed PbS nanocrystals with light sensitivity in the range of 350–2 000 nm (Figure 5(b))[136]. The photoresponsivity of the photodetector, distinguishing the color of the target, varied with the size of PbS nanocrystals in the system. Ghods et al. reported the bandgap modulation of two-dimensional WSe_2 flakes using Bi_2Se_3 NPs (Figure 5(c))[137]. The mixed-dimensional heterostructure comprising a topological insulator (Bi_2Se_3 NPs) and semiconductor (WSe_2) reported in this study showed excellent photoresponsivity in the visible range along with μs-scale IR absorption response speeds. Although NP incorporation enabled the facile tuning of the bandgap of photosensitive materials, its utilization in other functional devices, capable of detecting time-of-flight, motion, and polarized light, has not been developed to date. As visual sensors, the sensor-incorporated NPs primarily exhibited tunable optical properties through size, shape, and interparticle distance control, enhanced spectral diversity via bandgap modulation, and rapid photoresponse enabled by surface states. Given the esteemed ability of LAL, its facile modulation of optical properties is particularly suitable for providing reproducibility in multispectral photodetectors for advanced visual systems.

Several studies have attempted to develop gas sensors mimicking olfactory receptors for the detection of volatile organic and inorganic compounds[138–143]. NPs enhance the sensitivity, responsivity, and detection limits of gas sensors. Cho et al. reported single micro light emitting diode (μLED)-embedded chemoresistive sensors with time-variant illumination that could identify the various target gas species and their concentrations[144]. Coating the sensor surface with Au NPs induced the SPR effect, enhancing the reactivity and sensitivity of the sensor (Figure 5(d)). The Au-NP-based photocatalytic effect, represented by light absorption and the subsequent generation of hot electrons, enabled the sensors to release unique transient signals for each target gas under pulse illumination, facilitating selective gas detection with a single sensing device. Lee et al. also reported a high-performance gas-sensor array for indoor air-quality monitoring, which exhibited excellent sensing owing to the decoration of Au NPs on the surface of dome-like nanostructures

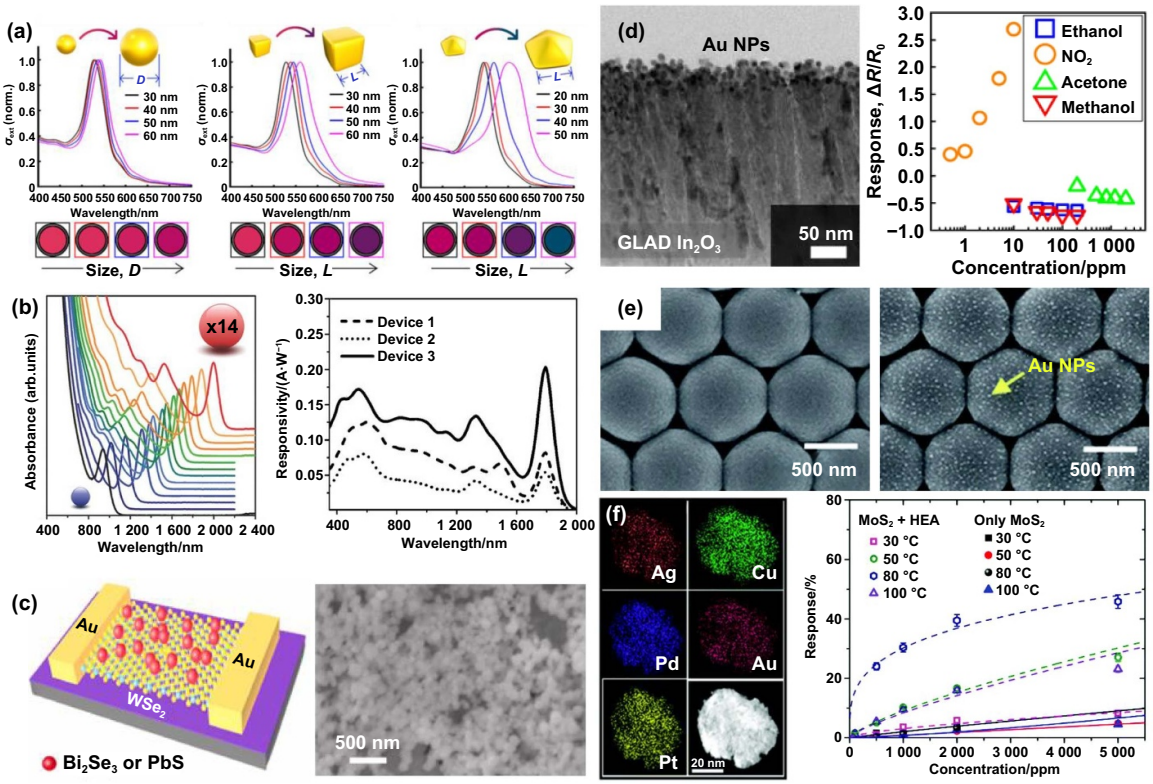

Figure 5. Application of NPs in optical and gas sensing. (a) Variations in the optical characteristics of Au NPs with their shape and size. Reproduced from[135]. CC BY 4.0. (b) Absorption spectra of PbS nanocrystals with different particle sizes, and the resultant photoresponsivity of ZnO/PbS/NiO broadband photodetectors. [136] John Wiley & Sons. © 2016 WILEY-VCH Verlag GmbH & Co. KGaA, Weinheim. (c) Schematics of WSe_2 photodetectors with Bi_2Se_3 NPs for selective-wavelength light detection, and SEM image of Bi_2Se_3 NPs. Reprinted from[137], © 2023 Elsevier Ltd. All rights reserved. (d) Cross-sectional TEM image of Au NPs deposited on a porous, columnar In_2O_3 sensing film, and the gas-sensing performance of devices toward various gaseous substances. Reproduced from[144]. CC BY 4.0. (e) Plain-view SEM images of a polystyrene-bead monolayer with NiO-based dome-like nanostructures (NDs) without and with Au NPs. Reproduced from[145] with permission from the Royal Society of Chemistry. (f) HAADF image with EDX elemental maps of $Au_{20}Ag_{20}Cu_{20}Pd_{20}Pt_{20}$ HEA NPs and comparison of the hydrogen gas sensing response of devices based on only MoS_2 and HEA NPs-decorated MoS_2. Reproduced from[146] with permission from the Royal Society of Chemistry.

(NDs) based on metal-oxide semiconductors[145]. Figure 5(e) presents the microscopic images of NiO NDs on polystyrene-bead monolayers with and without Au NPs, respectively. The incorporation of Au NPs expanded the depletion region of the metal-oxide semiconductors by facilitating the ionization of chemisorbed oxygen molecules, which enhanced the sensor response to gas molecules, including acetone, toluene, ammonia, and hydrogen sulfide, which could be distinguished by using array-type devices comprising three different oxide semiconductor NDs. Additionally, Urs et al. reported hydrogen gas sensors based on multi-component $Au_{20}Ag_{20}Cu_{20}Pd_{20}Pt_{20}$ HEA NPs decorating p-type MoS_2 sheet[146]. Figure 5(f) demonstrates the HAADF HR-TEM image with EDX elemental maps of the corresponding HEA NPs. The surface-enhanced Raman scattering effect of the HEA NPs lowered the work function of the MoS_2 multilayer, forming a Schottky barrier with contact electrode. The discrepancy in the surface chemical non-stoichiometry consequently enhanced the hydrogen gas sensing performance. Commonly, the NPs applied in olfactory sensors have enhanced sensitivity, responsivity, and detection limits through their high surface-to-volume ratio with catalytic activities and optical tunability with SPR effects. These unique properties allow olfactory sensors to identify and differentiate various gases, specifically enabled by surfactant-free metal-based NPs originating from LAL.

3.2. NP applications in gustatory and auditory sensors

Humans can identify and distinguish between five basic tastes: sweet, sour, salty, bitter, and umami[147]. When taste substances bind to the human tongue in a soluble state, the ion channels in the receptor cells instantaneously depolarize, releasing electrical signals that are transmitted to the brain through neural transport[147–150]. Artificial gustatory sensors that mimic the gustatory receptors in humans exhibit electrical responses to specific taste chemicals, such as sugars (sweat), acids (sour), sodium-based ionic compounds (salty), alkaloids or glycosides (bitter), and certain amino acids (umami). Various physicochemical sensors have been developed as artificial gustatory receptors, including electrochemical, optical, potentiometric, and microfluidic sensors; NP incorporation enhances the sensitivity, selectivity, and responsivity of these sensors[151–153].

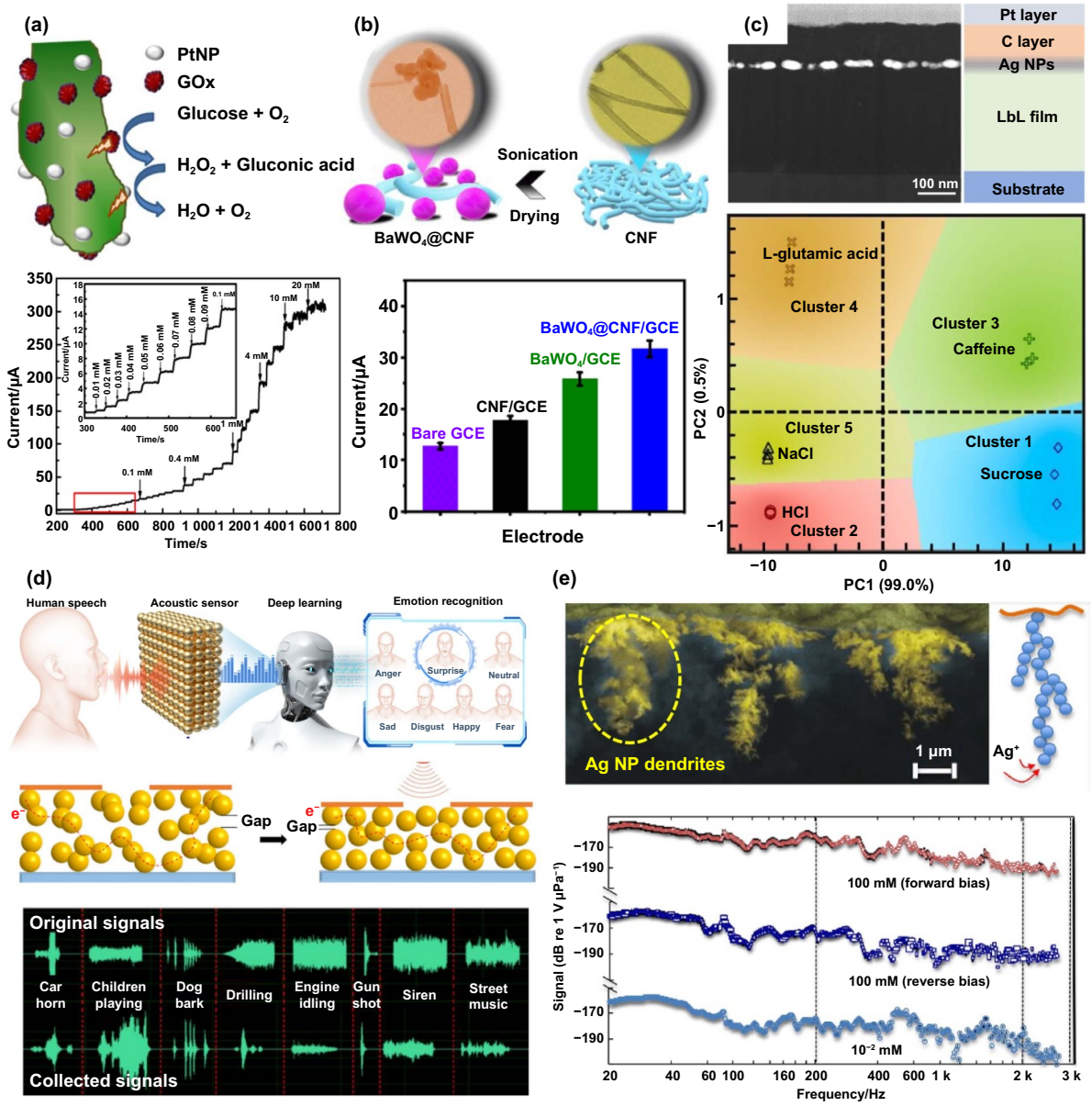

Figure 6. Application of NPs in artificial tongue and electronic ear sensors. (a) Schematics of a Pt NP–polyaniline hydrogel and surface-adhesive glucose oxidases; the electrical performance of the glucose sensor is leveraged by the glucose concentration. Reprinted with permission from[157]. Copyright (2013) American Chemical Society. (b) Schematics of $BaWO_4$ NP–carbon nanofiber nanocomposites and synergistic effect on enhancing the electrochemical sensitivity. Reprinted with permission from[159]. Copyright (2024) American Chemical Society. (c) Cross-sectional SEM image and schematics of devices comprising a layer-by-layer-derived polymer complex and Ag NPs for sensing various taste substances. Reprinted with permission from[154]. Copyright (2021) American Chemical Society. (d) Conceptual schematics of the piezoresistive artificial ear based on Au NP interfaces, capable of emotion recognition through deep learning. Comparison of original signals and sensor-collected signals while exposed to urban transportation noise. Reprinted with permission from[164]. Copyright (2024) American Chemical Society. (e) SEM image of hydrogel membrane implanted with a patch of silver dendrites (highlighted yellow), and schematic of a dendritic Ag NP network inside the hydrogel. The graph shows the frequency response of the hydrogel microphone at a low-frequency range (20–3 000 Hz), where salt concentration and bias direction affect the performance of the hydrogel microphone. Reproduced from[165]. CC BY 4.0.

Glucose sensors that mimic the biological mechanisms of sweet taste perception by detecting and quantifying glucose concentration use glucose oxidase to specifically recognize and catalyze glucose. This enzyme converts glucose into gluconolactone with the production of hydrogen peroxide (H_2O_2), which is detected electrochemically[154–156]. Zhai et al. reported a highly sensitive glucose sensor based on a Pt NP–polyaniline (Pt NP–PANI) composite matrix in which Pt NPs functioned as highly active catalysts for the electrooxidation of H_2O_2[157]. Figure 6(a) shows schematics of the Pt NP–PANI composite matrix with the oxidation of H_2O_2. The high density and homogeneous dispersion of Pt NPs within

the 3D nanostructured matrix of the polyaniline hydrogel significantly enhanced the performance of the glucose sensor, including its sensitivity, response speed, and detection limit, possibly owing to efficient electron transfer and a reduction in the diffusion distance of H_2O_2 molecules. Alencar et al. utilized copper chloride hydroxide hydrate (Cu-based) NPs with crumpled graphene for H_2O_2 detection; the crumpled graphene improved the electrical conductivity of the system and prevented NP agglomeration[158]. Empirically, catalytic NPs facilitated H_2O_2 reduction, lowered the detection limit, and increased the sensor sensitivity.

Meanwhile, Vinoth et al. developed a facile synthesis of $BaWO_4$ NP-integrated carbon nanofiber (CNF)[159]. They quantitatively detected TBR, a compound responsible for bitterness in coffee and dark chocolate, using an electrochemical technique that benefited from the promotion of active edge sites. Figure 6(b) illustrates schematics of $BaWO_4$@CNF nanocomposites and their synergistic effects on enhancing sensitivity. Additionally, Chen et al. reported the development of bitter-taste receptors comprising odorant-binding proteins (OBPs) from Drosophila melanogaster immobilized on screen-printed electrodes enhanced with Au NPs and reduced graphene oxide (rGO)[160]. The biosensor exhibited significant binding properties toward bitter molecules, including denatonium, quinine, and berberine, showing a linear response for analyte concentrations within 10^{-9}–10^{-6} mg·mL^{-1}. Besides providing an enlarged specific surface area for improved sensitivity, the Au NPs enabled the stable immobilization of OBPs through Au–S bonds, critical for the consistent and reliable detection of bitter molecules. Saraf et al. reported the design and development of a sensor for detecting limonin, a biomolecule that caused a bitter taste in citrus fruits[161]. In this sensor, redox-active ceria NPs underwent effective interactions with the active components of limonin, offering a rapid, sensitive, and on-site testing method for detecting the biomolecule. In addition to the detection of a single taste, versatile NPs enable the detection of multiple tastes, including sour, salty, and umami. Hensel et al. incorporated Ag NPs into layer-by-layer films comprising poly(allylamine hydrochloride) and poly(sodium 4-styrenesulfonate) placed on interdigitated electrodes to manufacture an electronic-tongue (e-tongue) sensing device[154]. Figure 6(c) shows the cross-sectional scheme of this sensing device. The controlled deposition of Ag NPs permitted precise adjustments to the electrical response, enabling the e-tongue to effectively differentiate basic tastes from various commercial umami-based flavors. Jia et al. reported a colorimetric sensor array based on amino acid-modified Au NPs (AA@Au NPs) that could differentiate between various types of baijiu[162]. The interaction of AA@Au NPs with various organic acids in baijiu resulted in NP aggregation and color changes, which enabled the rapid visual differentiation of baijiu samples based on their unique organic-acid profiles (i.e., their sour taste). Yu et al. reported the development of a bimetallic nanomaterial-based bionic taste sensor that mimicked the human taste system for evaluating the synergistic effects of umami substances[163]. The bimetallic nanomaterials (comprising MoS_2 and Pt–Pd NPs) enhanced the conductivity and catalytic properties of the sensor, enabling the detection of the binding of umami ligands to receptors, while the Au NPs ensured the stable attachment of the T1R1–Venus flytrap for precise detection. Consequently, this sensor could sensitively and specifically detect umami substances at extremely low concentrations. As gustatory sensors, NPs primarily enhanced sensitivity, selectivity, and responsivity by leveraging their catalytic properties, surface area control, and ability to facilitate electron transfer. For example, Pt NPs served as effective catalysts in glucose detection by promoting efficient electrooxidation of H_2O_2, while Au NPs stabilized odorant-binding proteins and enabled precise recognition of bitter molecules through Au–S bonds. Additionally, redox-active and bimetallic NPs optimized the detection of umami and sour tastes by modulating surface chemistry and electrical conductivity. These investigations imply that LAL-fabricated NPs, with their tunable size and reproducibility, are ideal candidates for scalable gustatory sensor arrays capable of detecting diverse taste profiles.

Several artificial electronics that mimic the human ear, including acoustic sensors and balancing sensors, have been developed[166–170]. Acoustic sensors mimic cochlea or hair cells and convert sounds or vibrations into electrical signals. Notably, sound can be categorized into three classes according to its frequency range: infrasound (<20 Hz), audible sound (20–20 000 Hz), and ultrasound (>20 000 Hz); audible sounds can be perceived by humans[171,172]. Based on the sensing mechanism, acoustic sensors can be further classified into piezoresistive, piezoelectric, electromagnetic, capacitive, triboelectric, and optical sensors[173–181]; versatile NPs can be easily grafted onto a variety of acoustic sensors[182–184]. Wang et al. developed a flexible piezoresistive artificial ear sensor based on Au NPs, which effectively converts acoustic signals into electrical outputs through resistance changes[164]. The sensors demonstrated a wide frequency response from 20 Hz to 12 kHz and detected sound signals up to 5 meters away, achieving classification accuracies over 95% for both emotional speech and urban noise using deep learning. The piezoresistive Au NP interface mimicked the tympanic membrane and cochlear functionality, with mechanical vibrations at the interface altering resistance, allowing real-time electrical signal conversion. Figure 6(d) depicts the conceptual schematics of sound recognition processes, the operational principle of the Au NP-based sensor, and signal comparisons qualifying the performance of the sensors. This design enabled applications such as emotion-based monitoring for healthcare and noise control in high-dB environments, showcasing the potential of NP-based acoustic sensors to enhance sensitivity and selectivity for advanced human-machine interfaces. Additionally, Park et al. reported a dual-mode, frequency-selective acoustic and haptic smart skin with high sensitivity, attributed to the utilization of triboelectric sensors with a hierarchical structure. The sensor showed a linear response over a broad frequency range, enabling the fabrication of advanced human-machine interfaces with noise-independent voice recognition and surface texture differentiation[172]. $BaTiO_3$ NPs within

the hierarchical macrodome/micropore structure of the ferroelectric composites in the system enhanced the dielectric properties of the triboelectric sensor and localized stress under mechanical deformation, leading to increased pressure sensitivity and frequency selectivity. This enabled the sensor to distinguish sounds across a wide range of frequencies (145–9 000 Hz). Gao et al. reported highly sensitive, cavity-free devices comprising hydrogel microphones embedded with Ag NPs for detecting low-frequency underwater sounds that showed excellent sensitivity on electric double-layer modulation[165]. Figure 6(e) shows the SEM image of the hydrogel membrane implanted with a patch of silver dendrites and the schematic of a dendritic Ag NP network inside the hydrogel membrane. The graph shows the frequency response of the hydrogel microphone at low-frequency range (20–3 000 Hz), where salt concentrations and bias direction affected the performance of the hydrogel microphone. The Ag NPs in the hydrogel microphones enhanced the device sensitivity by forming a deformable network that modulated capacitance in response to mechanical stimuli, such as sound waves, through electrode area and ion concentration variations. Yan et al. reported a fabric embedded with a piezoelectric fiber incorporating $BaTiO_3$ NPs, which functioned as a sensitive microphone by converting nanometer-scale mechanical vibrations from audible sound waves into electrical signals[177]. $BaTiO_3$ NPs enhanced the piezoelectric properties of the fiber by increasing its charge coefficient, thereby improving its sensitivity to mechanical vibrations and facilitating the efficient conversion of these vibrations into electrical signals.

Gyroscopic and accelerometric sensors have also been developed as artificial electronics that mimic the ear (i.e., E-ear systems)[185–188]. Magnetic NPs exhibit high potential applicability in gyroscopic sensors for balance perception owing to their unique functionality. Typically, these sensors contain iron oxide NPs, such as those comprising magnetite (Fe_3O_4), which exhibit strong magnetic moments and can be manipulated using external magnetic fields[189]. The orientation of Fe_3O_4 NPs can be altered by external forces, such as angular acceleration, resulting in detectable changes in the surrounding magnetic-field strength. By maintaining controlled magnetic-field intensity and frequency, the sensor can minimize phase delays and thermal agitation, ensuring the accurate detection of NP rotation. Moreover, the ability to finely tune the concentration and interactions of NPs within the sensor ensures a high measurement resolution, which is crucial for applications that require precise spatial awareness. Tang et al. utilized ZnO NPs embedded in a polyethyleneglycol (PEG) matrix as a sensitive strain-gauge element[190]. The resistance, capacitance, and impedance responses of low-cost accelerometers embedded with these gauge elements (based on PEG/ZnO NP nanocomposites) were measured under accelerations within 0–1 G. In artificial auditory sensors, the role of NPs mainly lay in enhancing sensitivity, frequency selectivity, and detection accuracy by leveraging their dielectric, piezoelectric, and magnetic properties. These NPs improved sound wave conversion and frequency-specific responses in acoustic sensors, enhanced sensitivity to low-frequency underwater sounds within deformable networks, and facilitated precise balance perception. With size controllability and enhanced surface properties, LAL-derived NPs are highly promising for developing high-sensitivity, frequency-selective auditory sensors tailored for advanced human-machine interfaces, and precise spatial awareness applications.

3.3. NP applications in tactile sensors

The versatility of NPs also enables the fabrication of high-sensitivity artificial tactile sensors that detect a variety of perceptions, including touch, pressure, vibration, strain, temperature, and humidity[191–196]. Yoo et al. reported the development of an industrial-grade, bending-insensitive, transparent nanoforce touch sensor with a hierarchical nanocomposite film consisting of nanostructured plastic-based coplanar electrodes and a dielectric polymer layer embedded with Ag NPs[197]. Incorporating NPs resulted in a significant increase in the dielectric constant of the SU-8 polymer layer, ensuring high device sensitivity owing to the percolation effect because of which density changes in Ag NPs under pressure led to a significant change in capacitance. This effect was amplified by the stress concentration within the nanograting structures of the nanostructure plastic base (Figure 7(a)), resulting in improved sensitivity, even with a low concentration of NPs, while maintaining high transparency and flexibility. An ultrahigh-resolution pressure sensor based on percolative Pd NP arrays reported by Chen et al. demonstrated a sensitivity of 0.13 kPa^{-1} and resolution of 0.5 Pa owing to the operation of a quantum-tunneling transport mechanism, enabling the development of devices such as barometric altimeters with a resolution of 1 meter[198]. This sensor detected pressure variations approximately 2 000 times lower than the perception threshold of human skin, which typically denotes pressure changes in the range of 1–2 kPa. A cost-effective and low-voltage flexible sensing platform based on monolayer-capped nanoparticles (MCNPs) reported by Segev-Bar et al. could detect pressure, temperature, and humidity[199]. The MCNPs facilitated electron tunneling mechanisms, which resulted in electrical resistance changes based on the interparticle distance, imparting the system with high sensitivity toward environmental parameters. This innovative study confirmed the high potential of MCNP-based sensors, which showed tunable sensitivity and robust performance, even after extensive bending cycles, for advanced electronic-skin applications.

In addition to pressure and touch sensors, NPs have found their utility in strain-gauge sensors[200,201]. Ketelsen et al. reported the development of highly sensitive strain gauges comprising 1, 9 nonanedithiol cross-linked Au NP networks[202]. The primary sensing material of this device, Au NPs, exhibited high sensitivity toward strain through a mechanism based on the tunneling of charge carriers between particles, which caused electrical resistance changes. Figure 7(b) shows the photographic devices with SEM image demonstrating the cross-linked Au NP networks.

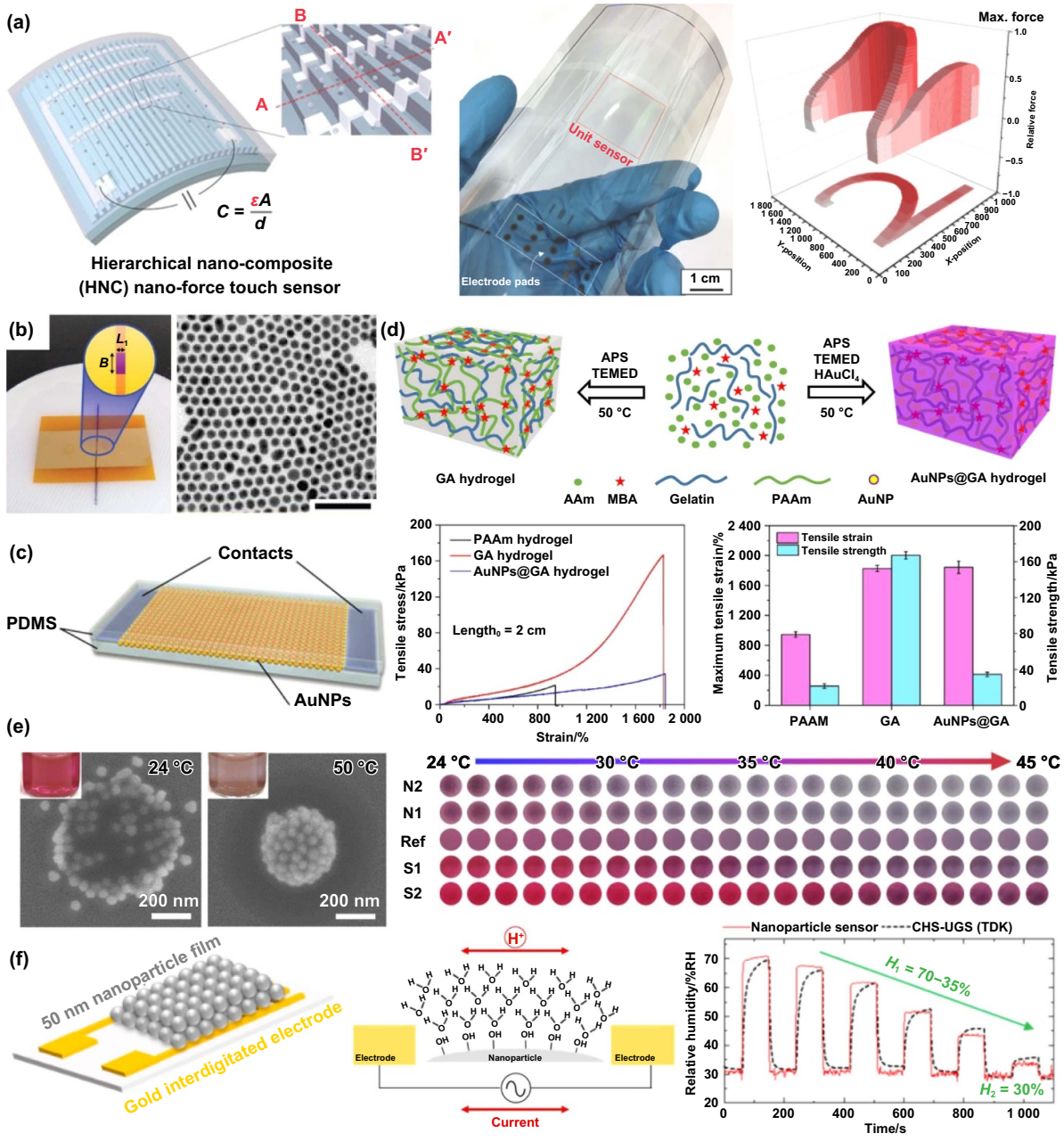

Figure 7. Application of NPs in tactile sensors, including pressure, strain, temperature, and humidity sensing. (a) Schematics of a hierarchical nanocomposite film-based touch sensor with cross-sections cut parallel and perpendicular to the direction of the electric field along with the force mapping recorded using a smart phone. [197] John Wiley & Sons. © 2018 WILEY-VCH Verlag GmbH & Co. KGaA, Weinheim. (b) Photographs of the strain sensor and SEM image of the cross-linked Au NPs. Reproduced with permission from[202]. © 2022 The Authors. Advanced Functional Materials published by Wiley-VCH GmbH. CC BY-NC 4.0. (c) Schematics of the strain sensor based on Au NP layer sandwiched between polydimethylsiloxane (PDMS) layers. Reprinted with permission from[203]. Copyright (2021) American Chemical Society. (d) Incorporation of Au NPs into gelatin-based hydrogel network, and the sensing performance of devices with different conditions. Reprinted from[205], © 2021 Elsevier B.V. All rights reserved. (e) SEM images of temperature-dependent Au NPs decorated with poly(N-isopropylacrylamide) microgels along with the color distribution. Reproduced from[206]. CC BY 4.0. (f) Schematics of SiO_2 NP-based humidity sensors and the relevant proton conduction mechanism with the humidity sensing performance. Reproduced from[209]. CC BY 4.0.

Owing to anisotropic strain sensitivity, these strain gauges were integrated into a flexible polymer. Additionally, Jheng et al. reported Au NP-based strain sensors[203]. Figure 7(c) presents the schematic of the device comprising Au NP thin-film sensing layers deposited on flexible and stretchable polydimethylsiloxane (PDMS) substrates that could measure low pressures with a responsivity of 3.3 kPa^{-1}. A stretchable strain sensor based on Ag NP thin films reported by Lee et al. was able to detect both tensile and compressive strains; these systems were easily transferred onto PDMS substrates

by a streamlined single-step direct-transfer process[204]. Zhang et al. also reported the development of Janus adhesive-tough hydrogels incorporating in-situ generated Au NPs within a gelatin-polyacrylamide double network structure[205]. The incorporated Au NPs disrupted the triple helix structure of the gelatin on the adhesive side, enhancing both interfacial bonding and flexibility, which enabled the synergistic balance of strong adhesion and mechanical toughness. As shown in Figure 7(d), the Au NPs-incorporating hydrogels exhibited significantly enhanced strain at the break while slightly compromising tensile strength due to the disrupted network structure.

NPs can also be used to perceive other senses such as temperature and humidity. Choe et al. reported the development of a smart colorimetric patch based on thermoresponsive plasmonic microgels embedded in stretchable hydrogel film[206]. The Au NPs decorated with poly(N-isopropylacrylamide) (PNIPAM) microgels showed large and reversible color shifts owing to efficient plasmon coupling between the Au NPs (Figure 7(e)). This device enabled rapid temperature visualization with a high resolution of 0.2 °C over a broad temperature range of 25 °C–40 °C, exhibiting high potential applicability in wearable sensors and soft robotics. Other studies also reported PNIPAM-decorated Au NPs that functioned as colorimetric temperature sensors[207]. Additionally, Liu et al. reported charged colloidal Au NPs capped with strong ligands, such as bis(*p*-sulfonatophenyl)-phenylphosphine, that underwent assembly and disassembly in aqueous solution in response to temperature changes[208]. In this system, manipulating electrostatic interactions through the temperature-dependent zeta potential of the charged NPs enabled the reversible thermoresponsive tuning of plasmon coupling. NPs are also effective in tracing the humidity of ambient air. Nonporous SiO_2 NP-based humidity sensors developed by Kano et al. featured excellent chemical stability and a rapid response time (i.e., a hysteresis error of 2% at 85 RH% and response/recovery times of 2.8/2.3 s, respectively)[209]. In this system, the NPs formed multilayer water films on the surface and facilitated proton conduction through hydrogen bonds, altering the active-layer resistance with changes in humidity (Figure 7(f)). Similarly, Yadav et al. demonstrated that non-functionalized Au NPs enabled high-performance humidity sensing owing to their high specific surface area and the presence of surface cracks[210]. This study highlights the ability of Au NPs to enable stable and repeatable humidity sensing, despite the lack of functionalization. NPs play a critical role in advanced tactile sensors by enhancing sensitivity, flexibility, and responsiveness across multiple sensing modalities such as pressure, strain, temperature, and humidity. Their unique properties, including tunable dielectric constants, quantum tunneling mechanisms, and large specific surface areas, enable precise perception and differentiation of environmental stimuli. The scalability, tunability, and surface modification flexibility provided by LAL-derived NPs make them exceptionally well-suited for the development of high-performance tactile sensors, ensuring robust and efficient operation in wearable technologies and electronic-skin systems.

3.4. NP applications in synaptic devices

Artificial synaptic devices have emerged as pivotal innovations for emulating the complex functionalities of the human brain within electronic systems. These devices are designed to replicate the dynamic synaptic connections between neurons and perform cognitive processes of brain, such as memorizing and learning. Various device platforms that emulate biological synapses, where perceptible stimuli serve as presynaptic spikes, typically represented as pulse biases, have been proposed. Additionally, innovative nanotechnologies and advanced materials have enabled the development of synaptic devices with efficient and low-power computations. This section reviews some recently developed NP-based synaptic devices.

Guo et al. reported a diffusive artificial synapse using Au NPs functionalized with charged self-assembled monolayers, showing switching characteristics analogous to biological Ca^{2+} dynamics and emulating key synaptic functions[211]. Au NP incorporation resulted in a diffusive memristor, wherein mobile counterions responded to the electric field and diffused back upon removal (Figure 8(a)). Zeng et al. also investigated the applicability of ZnO NPs integrated into ZTO films in phototransistors that could emulate the neural coding of the human visual system[212]. Gate-voltage modulation resulted in distinct positive and negative paired-pulse ratios, attributed to oxygen adsorption/desorption and electron trapping at the ZnO NP/SiO_2 interface. Neuromorphic transistors with Au NP-decorated indium tin oxide fibers, developed by Sim et al., mimicked the real-time light sensing and signal transduction of retinal neurons, showing biologically accurate simulations of light-intensity adjustments[213]. Furthermore, Jiang et al. developed neuromorphic motion-cognition systems comprising SnO_2 NP-doped MoS_2 thin films[214]. In this system, the enhanced charge-trapping effect arising from SnO_2 NPs was coupled with an improvement in the electrostatic gating capability of the device. A paper by Kim et al. demonstrated the precise modulation of synaptic plasticity using an Al-NP-embedded indium gallium zinc oxide (IGZO) synaptic transistor, which emulated essential synaptic functions and supported the implementation of neuromorphic computing systems[215]. The density of the Al NPs within the IGZO channel modulated the conductance states, enabling precise control over synaptic plasticity, including the excitatory and inhibitory postsynaptic currents, paired-pulse facilitation, and both short- and long-term synaptic plasticity (Figure 8(b)). This fine-tuning capability is essential for neuromorphic computing applications because it facilitates the reliable emulation of synaptic behavior, thereby facilitating high accuracy in tasks such as image recognition and learning. Liu et al. reported a significant advancement in nanomemristors, demonstrating ultralow switching voltages down to 4 mV using surface-modified Cu NPs[216]. The Cu NPs were functionalized with dalkyl-dithiophosphoric to form a 400-nm-thick layer, achieving volatile threshold-type resistive switching with minimal power consumption (Figure 8(c)). Due to the surface modification, Cu NPs could stabilize their

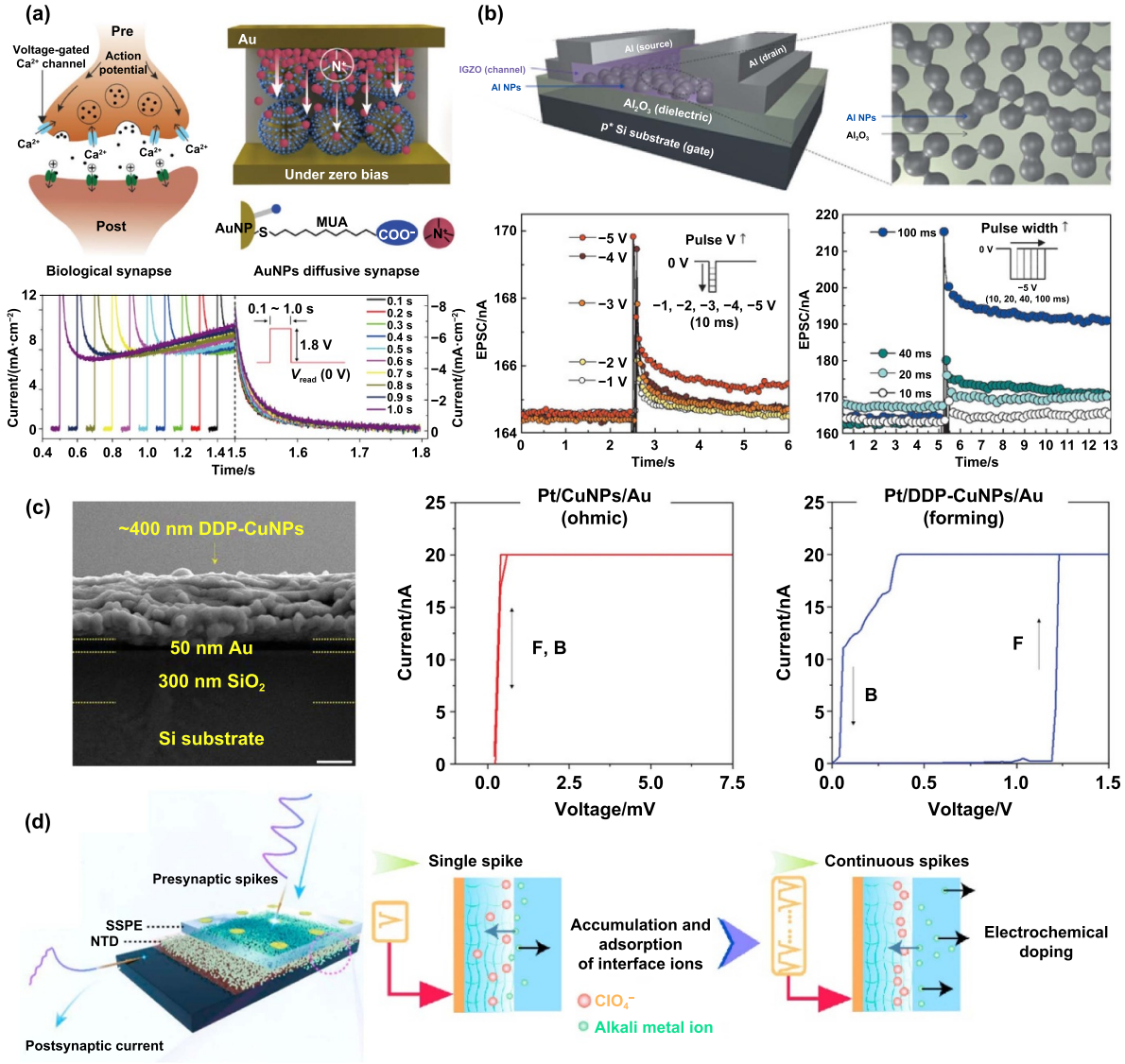

Figure 8. NP-based artificial synaptic devices. (a) Schematics of biological and NP-based artificial synapses. The graph shows the transient current under varied pulse widths within 0.1–1.0 s. Reprinted with permission from[211]. Copyright (2024) American Chemical Society. (b) Schematics of a synaptic transistor comprising an indium gallium zinc oxide (IGZO) layer embedded with Al NPs. Excitatory postsynaptic current (EPSC) responses of the synaptic transistor with leveraged gate-voltage amplitudes and pulse widths. [215] John Wiley & Sons. © 2020 WILEY-VCH Verlag GmbH & Co. KGaA, Weinheim. (c) Cross-sectional SEM image of surface-modified Cu NP film deposited on Au film, and comparison of electrical characteristics of synaptic devices depending on the surface modification. [216] John Wiley & Sons. © 2022 Wiley-VCH GmbH. (d) Schematics of a synaptic device based on a sodium-based solid polymer electrolyte, the ion-storage mechanisms of the artificial synapses based on Na^+ and Li^+, and images of 2 pixel × 3 pixel encoded by different amplitudes, rates, and durations using a 6-synapse unit. Reprinted from[217], © 2020 Elsevier Ltd. All rights reserved.

dispersion and create Schottky barriers that induce insulator-to-metal transitions, with reliable switching capability over hundreds of cycles. Two-terminal sodium ion artificial synapse systems with an NP/electrolyte architecture, first reported by Wei et al., emulated biological synapse behaviors, showing essential synaptic functions such as postsynaptic currents and paired-pulse facilitation with ultra-low-power consumption along with pain perception and dendritic integration abilities[217]. TiO_2 NPs in such systems functioned as effective Na reservoirs, facilitating ion migration and electrochemical doping to replicate synaptic plasticity and enhance postsynaptic responses. With an ultra-low-power consumption of 0.55 pW per synaptic event, this architecture supported advanced functionalities, such as pain perception and dendritic integration, making it a promising component of high-performance bioinspired flexible neural systems (Figure 8(d)). Several other studies reported the versatility of NP systems for synaptic behavior. SnO_2 NPs with poly(3-hexylthiophene-2,5-diyl) nanowires enhanced photoelectric responsiveness and bidirectional plasticity[218] and SnO_2 NP-based synaptic transistors permitted electrochemical doping to modulate synaptic weight[219]. Chen et al. also reported the undesired neurotoxic effects of NPs[152]. ZnO NPs could traverse the tongue-brain pathway owing to their high biological activity and small size,

leading to neuroinflammation and subsequent synaptic transmission deficits. These NPs activated the JAK-STAT signaling pathway, which in turn inhibited the Neurexin1–PSD95–Neuroloigin1 pathway and reduced c-fos expression, resulting in impaired taste perception. NP-based synaptic devices require key attributes such as efficient charge trapping, controlled ion migration, and tunable conductance states to replicate essential synaptic functions, including plasticity, learning, and memory. Their integration enables low-power operations, fine-tuning of synaptic weights, and reliable emulation of biological processes. LAL-derived NPs are particularly suitable for these devices due to their controllable size, high surface reactivity, and scalable fabrication potential, allowing precise customization and reliable performance in neuromorphic systems for next-generation artificial intelligence.

4. Summary and outlook

This review comprehensively summarizes recent advances in LAL and NP-incorporated ASS devices to provide useful resources for future research on high-performance, reliable ASS electronics. Recent advances in LAL addressed the inherent scalability issues, and their abilities to produce surfactant-free NPs ensure the controllability of size and composition even without high temperatures, vacuum conditions, or complex chemical processes. The fundamental mechanisms and key parameters influencing the characteristics of NPs were deeply discussed. Laser fluence affects the ablation rate and NP yield, with higher fluences typically producing smaller NPs owing to increased fragmentation. The laser wavelength affects energy transfer efficiency, thereby affecting the size and colloidal density of the resultant NPs. Shorter wavelengths typically result in smaller NPs with higher colloidal densities. The pulse duration influences the ablation mechanism and NP features, with shorter pulses favoring higher productivity and smaller NPs. The repetition rate and liquid medium properties also influence the NP characteristics and production efficiency significantly. Despite these explorations, understanding of the intertwined interplay still lacks, necessitating more experimental investigations. Subsequently, the advantages of metal-based NPs in ASS devices, particularly perceptual sensors and synaptic devices, were comprehensively reviewed. These NPs improved the sensitivity, selectivity, and efficiency of perceptual sensors, while offering unexpected synaptic functions and enhancing memorial performance for artificial synapses.

Despite the promises of LAL with distinct NPs, their electronic application, particularly in sensory and synaptic devices, remains largely unexplored. This can be attributed to several factors. First, the process of separating and purifying NPs to ensure the target quality and characteristics is challenging; inadequate purification can lead to inconsistent NP quality and performance variations in sensory systems. Second, preventing aggregation during storage is crucial for maintaining the functional properties of NPs; however, effective storage systems that prevent aggregation are currently lacking. Third, considering the material-specific properties of NPs, certain metal targets remain costly, particularly those with high purity or specialized compositions. This cost concern is closely tied to increased production expenses in industrial settings, limiting their broader adoption and commercialization in advanced ASS applications. Addressing these challenges requires the development of advanced separation and purification techniques, innovative storage solutions, cost-effective production methods, and collaborative research.

To address the previously mentioned challenges and enhance the application of LAL-fabricated NPs in ASS, developing advanced separation and purification techniques to ensure consistent NP quality using methods such as centrifugation, filtration, and electrophoresis is vital. Additionally, future research should focus on designing innovative storage solutions that prevent NP aggregation through the use of stabilizing agents and controlled environments for maintaining NP stability. Exploring cost-effective production methods, such as using economic raw materials and recycling metal targets, can mitigate the economic barriers associated with LAL processes. Moreover, collaborative research between academic institutions, industries, and government agencies is essential for accelerating the development and commercialization of these technologies. These perspectives highlight the potential of ASS for enabling seamless integration into human skin, such as skin-conformal sensory and synaptic devices, providing immersive and interactive experiences in metaverse technologies while fostering industrial and technological advancements.

Acknowledgments

This work was supported by the Nano & Material Technology Development Program through the National Research Foundation of Korea (NRF) and was funded by the Ministry of Science and ICT (Grant Nos. RS-2024-00403639 and RS-2024-00411904).

Conflict of interest

The authors declare that they have no competing financial interests or personal relationships that may have influenced the work reported in this study.

References

[1] Wu D P, Yang Z G, Zhang P N, Wang R Y, Yang B R and Ma X Q. 2023. Virtual-reality interpromotion technology for metaverse: a survey. *IEEE Internet Things J.* **10**, 15788–15809.

[2] Xi N N, Chen J, Gama F, Riar M and Hamari J. 2023. The challenges of entering the metaverse: an experiment on the effect of extended reality on workload. *Inf. Syst. Front.* **25**, 659–680.

[3] Dudley J, Yin L L, Garaj V and Kristensson P O. 2023. Inclusive immersion: a review of efforts to improve accessibility in virtual reality, augmented reality and the metaverse. *Virtual Real.* **27**, 2989–3020.

[4] Wedel M, Bigné E and Zhang J. 2020. Virtual and augmented reality: advancing research in consumer marketing. *Int. J. Res. Mark* **37**, 443–465.
[5] Sánchez-Cabrero R, Costa-Román Ó, Pericacho-Gómez F J, Novillo-López M Á, Arigita-García A and Barrientos-Fernández A. 2019. Early virtual reality adopters in spain: sociodemographic profile and interest in the use of virtual reality as a learning tool. *Heliyon* **5**, e01338.
[6] Masteller A, Sankar S, Kim H B, Ding K Q, Liu X G and All A H. 2021. Recent developments in prosthesis sensors, texture recognition, and sensory stimulation for upper limb prostheses. *Ann. Biomed. Eng.* **49**, 57–74.
[7] Shull P B and Damian D D. 2015. Haptic wearables as sensory replacement, sensory augmentation and trainer—a review. *J. Neuroeng. Rehabil.* **12**, 59.
[8] Bach-Y-Rita P, Collins C C, Saunders F A, White B and Scadden L. 1969. Vision substitution by tactile image projection. *Nature* **221**, 963–964.
[9] Maidenbaum S, Abboud S and Amedi A. 2014. Sensory substitution: closing the gap between basic research and widespread practical visual rehabilitation. *Neurosci. Biobehav. Rev.* **41**, 3–15.
[10] Zeng F G, Rebscher S, Harrison W, Sun X A and Feng H H. 2008. Cochlear implants: system design, integration, and evaluation. *IEEE Rev. Biomed. Eng.* **1**, 115–142.
[11] Eshraghi A A, Nazarian R, Telischi F F, Rajguru S M, Truy E and Gupta C. 2012. The cochlear implant: historical aspects and future prospects. *Anat. Rec.* **295**, 1967–1980.
[12] Li Y, Wei X Y, Zhou Y M, Wang J and You R. 2023. Research progress of electronic nose technology in exhaled breath disease analysis. *Microsyst. Nanoeng.* **9**, 129.
[13] Wilson A D. 2012. Review of electronic-nose technologies and algorithms to detect hazardous chemicals in the environment. *Proc. Technol.* **1**, 453–463.
[14] Becher C, Kaul P, Mitrovics J and Warmer J. 2010. The detection of evaporating hazardous material released from moving sources using a gas sensor network. *Sens. Actuators B* **146**, 513–520.
[15] Tahara Y and Toko K. 2013. Electronic tongues–a review. *IEEE Sens. J.* **13**, 3001–3011.
[16] Vahdatiyekta P, Zniber M, Bobacka J and Huynh T P. 2022. A review on conjugated polymer-based electronic tongues. *Anal. Chim. Acta* **1221**, 340114.
[17] Fayaz U, Srivastava S, Dar A H, Bashir I, Manzoor S, Pandey V K, Shams R and Dash K K. 2024. Recent insights into E-tongue interventions in food processing applications: an updated review. *Curr. Food Sci. Technol. Rep.* **2**, 169–182.
[18] Bang J et al. 2024. Bioinspired electronics for intelligent soft robots. *Nat. Rev. Electr. Eng.* **1**, 597–613.
[19] Fu X M, Cheng W, Wan G X, Yang Z J and Tee B C K. 2024. Toward an AI era: advances in electronic skins. *Chem. Rev.* **124**, 9899–9948.
[20] Boahen E K, Kweon H, Oh H, Kim J H, Lim H and Kim D H. 2025. Bio-inspired neuromorphic sensory systems from intelligent perception to nervetronics. *Adv. Sci.* **12**, 2409568.
[21] Wang D X, Guo Y, Liu S Y, Zhang Y R, Xu W L and Xiao J. 2019. Haptic display for virtual reality: progress and challenges. *Virtual Real. Intell. Hardw* **1**, 136–162.
[22] Bag A, Ghosh G, Sultan M J, Chouhdry H H, Hong S J, Trung T Q, Kang G Y and Lee N E. 2024. Bio-inspired sensory receptors for artificial-intelligence perception. *Adv. Mater.* 2403150.
[23] Jiang C P, Liu J Q, Yang L, Gong J D, Wei H H and Xu W T. 2022. A flexible artificial sensory nerve enabled by nanoparticle-assembled synaptic devices for neuromorphic tactile recognition. *Adv. Sci.* **9**, 2106124.
[24] Wang J F, Suo J, Song Z X, Li W J and Wang Z B. 2023. Nanomaterial-based flexible sensors for metaverse and virtual reality applications. *Int. J. Extrem. Manuf.* **5**, 032013.
[25] Bi P, Liu X W, Yang Y, Wang Z Y, Shi J, Liu G M, Kong F F, Zhu B P and Xiong R. 2019. Silver-nanoparticle-modified polyimide for multiple artificial skin-sensing applications. *Adv. Mater. Technol.* **4**, 1900426.
[26] Alibart F, Pleutin S, Bichler O, Gamrat C, Serrano-Gotarredona T, Linares-Barranco B and Vuillaume D. 2012. A memristive nanoparticle/organic hybrid synapstor for neuroinspired computing. *Adv. Funct. Mater.* **22**, 609–616.
[27] Amendola V, Amans D, Ishikawa Y, Koshizaki N, Scirè S, Compagnini G, Reichenberger S and Barcikowski S. 2020. Room-temperature laser synthesis in liquid of oxide, metal-oxide core-shells, and doped oxide nanoparticles. *Chemistry* **26**, 9206–9242.
[28] Machac P, Cichon S, Lapcak L and Fekete L. 2020. Graphene prepared by chemical vapour deposition process. *Graphene Technol.* **5**, 9–17.
[29] Wu Q K, Wongwiriyapan W, Park J H, Park S, Jung S J, Jeong T, Lee S, Lee Y H and Song Y J. 2016. *In situ* chemical vapor deposition of graphene and hexagonal boron nitride heterostructures. *Curr. Appl. Phys.* **16**, 1175–1191.
[30] Yuan Y W, Zhang F H, Wang H, Liu J L, Zheng Y Q and Hou S F. 2017. Chemical vapor deposition graphene combined with Pt nanoparticles applied in non-enzymatic sensing of ultralow concentrations of hydrogen peroxide. *RSC Adv.* **7**, 30542–30547.
[31] Song O et al. 2022. All inkjet-printed electronics based on electrochemically exfoliated two-dimensional metal, semiconductor, and dielectric. *NPJ 2D Mater. Appl.* **6**, 64.
[32] Wu L et al. 2017. Improving the stability and size tunability of cesium lead halide perovskite nanocrystals using trioctylphosphine oxide as the capping ligand. *Langmuir* **33**, 12689–12696.
[33] Wang Y T, Zhang X T, Xu J B, Shen Y, Wang C A, Li F W, Zhang Z H, Chen J, Ye Y H and Shen R Q. 2021. Fabrication and characterization of Al–CuO nanocomposites prepared by sol-gel method. *Def. Technol.* **17**, 1307–1312.
[34] Wu Y H, Wang Z Q, Chen S S, Wu J N, Guo X H and Liu Z Y. 2015. One-step hydrothermal synthesis of silver nanoparticles loaded on N-doped carbon and application for catalytic reduction of 4-nitrophenol. *RSC Adv.* **5**, 87151–87156.
[35] Kumar P, Khanduri H, Pathak S, Singh A, Basheed G A and Pant R P. 2020. Temperature selectivity for single phase hydrothermal synthesis of PEG-400 coated magnetite nanoparticles. *Dalton Trans.* **49**, 8672–8683.
[36] Mohan S, Vellakkat M, Aravind A and Reka U. 2020. Hydrothermal synthesis and characterization of Zinc Oxide nanoparticles of various shapes under different reaction conditions. *Nano Express* **1**, 030028.
[37] Sedira S and Mendaci B. 2020. Hydrothermal synthesis of spherical carbon nanoparticles (CNPs) for supercapacitor electrodes uses. *Mater. Renew. Sustain. Energy* **9**, 1.
[38] Zhao B A, Cai W F, Pu K B, Bai J R, Gao J Y and Wang Y H. 2022. Electrochemical deposition of flower-like nanostructured silver particles with a PVA modified carbon cloth cathode. *RSC Adv.* **12**, 21793–21800.
[39] Weber C J, Strom N E and Simoska O. 2024. Electrochemical deposition of gold nanoparticles on carbon ultramicroelectrode arrays. *Nanoscale* **16**, 16204–16217.
[40] Meng Q L, Wang Z B, Chai X Y, Weng Z K, Ding R and Dong L T. 2016. Fabrication of hematite (α-Fe_2O_3) nanoparticles using electrochemical deposition. *Appl. Surf. Sci.* **368**, 303–308.
[41] Bhattacharjee K and Prasad B L V. 2023. Surface functionalization of inorganic nanoparticles with ligands: a necessary step for their utility. *Chem. Soc. Rev.* **52**, 2573–2595.

[42] Behera P and De M. 2024. Surface-engineered nanomaterials for optical array based sensing. *ChemPlusChem* **89**, e202300610.
[43] Riahi F, Doñate-Buendia C, Barcikowski S and Gökce B. 2024. How nanoparticle size and bubble merging is governed by short-range spatially controlled double-beam laser ablation in liquids. *Part. Part. Syst. Charact.* **41**, 2300145.
[44] Fromme T, Tintrop L K, Reichenberger S, Schmidt T C and Barcikowski S. 2023. Impact of chemical and physical properties of organic solvents on the gas and hydrogen formation during laser synthesis of gold nanoparticles. *ChemPhysChem* **24**, e202300089.
[45] Waag F, Streubel R, Gökce B and Barcikowski S. 2021. Synthesis of gold, platinum, and gold-platinum alloy nanoparticle colloids with high-power megahertz-repetition-rate lasers: the importance of the beam guidance method. *Appl. Nanosci.* **11**, 1303–1312.
[46] Barcikowski S, Amendola V, Lau M, Marzun G, Rehbock C, Reichenberger S, Zhang D S and Gökce B. 2019. *Handbook of Laser Synthesis & Processing of Colloids*. 2nd edn (University of Duisburg-Essen) p 218.
[47] Ziefuss A, Barcikowski S and Zhigilei L V. 2022. Advances in pulsed laser synthesis of nanoparticles in liquids. *Sci. China Phys. Mech. Astron.* **65**, 274201.
[48] Heine N, Doll-Nikutta K, Stein F, Jakobi J, Ingendoh-Tsakmakidis A, Rehbock C, Winkel A, Barcikowski S and Stiesch M. 2024. Anti-biofilm properties of laser-synthesized, ultrapure silver–gold-alloy nanoparticles against *Staphylococcus aureus*. *Sci. Rep.* **14**, 3405.
[49] Luo R C, Neu B and Venkatraman S S. 2012. Surface functionalization of nanoparticles to control cell interactions and drug release. *Small* **8**, 2585–2594.
[50] Damma D and Smirniotis P G. 2020. $FeCeO_x$ supported Ni, Sn catalysts for the high-temperature water–gas shift reaction. *Catalysts* **10**, 639.
[51] Putri L A, Prabowo Y D, Dewi D M M, Mumtazah Z, Adila F P, Fadillah G, Amrillah T, Triyana K, Nugroho F A A and Wasisto H S. 2024. Review of noble metal nanoparticle-based colorimetric sensors for food safety monitoring. *ACS Appl. Nano Mater.* **7**, 19821–19853.
[52] Waag F, Fares W I M A, Li Y, Andronescu C, Gökce B and Barcikowski S. 2022. Identification of the main mixing process in the synthesis of alloy nanoparticles by laser ablation of compacted micropowder mixtures. *J. Mater. Sci.* **57**, 3041–3056.
[53] Lin Z, Yue J, Liang L, Tang B, Liu B, Ren L, Li Y and Jiang L L. 2020. Rapid synthesis of metallic and alloy micro/nanoparticles by laser ablation towards water. *Appl. Surf. Sci.* **504**, 144461.
[54] Compagnini G, Messina E, Puglisi O and Nicolosi V. 2007. Laser synthesis of Au/Ag colloidal nano-alloys: optical properties, structure and composition. *Appl. Surf. Sci.* **254**, 1007–1011.
[55] Nyabadza A, Vazquez M and Brabazon D. 2023. A review of bimetallic and monometallic nanoparticle synthesis via laser ablation in liquid. *Crystals* **13**, 253.
[56] Zerebecki S et al. 2022. Engineering of cation occupancy of $CoFe_2O_4$ oxidation catalysts by nanosecond, single-pulse laser excitation in water. *ChemCatChem* **14**, e202101785.
[57] Budiyanto E et al. 2021. Impact of single-pulse, low-intensity laser post-processing on structure and activity of mesostructured cobalt oxide for the oxygen evolution reaction. *ACS Appl. Mater. Interfaces* **13**, 51962–51973.
[58] Spellauge M, Tack M, Streubel R, Miertz M, Exner K S, Reichenberger S, Barcikowski S, Huber H P and Ziefuss A R. 2023. Photomechanical laser fragmentation of IrO_2 microparticles for the synthesis of active and redox-sensitive colloidal nanoclusters. *Small* **19**, 2206485.
[59] Kumar S and Kumar M. 2024. Utilizations of high entropy alloy nanoparticles for gas sensors. *Trans. Indian Natl Acad. Eng.* **9**, 679–687.
[60] Gao S J, Hao S Y, Huang Z N, Yuan Y F, Han S, Lei L C, Zhang X W, Shahbazian-Yassar R and Lu J. 2020. Synthesis of high-entropy alloy nanoparticles on supports by the fast moving bed pyrolysis. *Nat. Commun.* **11**, 2016.
[61] Yao Y G et al. 2022. High-entropy nanoparticles: synthesis-structure-property relationships and data-driven discovery. *Science* **376**, eabn3103.
[62] Wang F X, Feng X, Gao Y T, Ding X, Wang W and Zhang J. 2023. Green synthesis of PtPdNiFeCu high-entropy alloy nanoparticles for glucose detection. *ACS Omega* **8**, 47773–47780.
[63] Mondal B, Zhang X L, Kumar S, Long F, Katiyar N K, Kumar M, Goel S and Biswas K. 2023. A resistance-driven H_2 gas sensor: high-entropy alloy nanoparticles decorated 2D MoS_2. *Nanoscale* **15**, 17097–17104.
[64] Fazio E et al. 2020. Nanoparticles engineering by pulsed laser ablation in liquids: concepts and applications. *Nanomaterials* **10**, 2317.
[65] Dell'Aglio M, Gaudiuso R, De Pascale O and De Giacomo A. 2015. Mechanisms and processes of pulsed laser ablation in liquids during nanoparticle production. *Appl. Surf. Sci.* **348**, 4–9.
[66] Amans D, Cai W P and Barcikowski S. 2019. Status and demand of research to bring laser generation of nanoparticles in liquids to maturity. *Appl. Surf. Sci.* **488**, 445–454.
[67] Shabalina A V, Svetlichnyi V A and Kulinich S A. 2022. Green laser ablation-based synthesis of functional nanomaterials for generation, storage, and detection of hydrogen. *Curr. Opin. Green Sustain. Chem.* **33**, 100566.
[68] Yang C, Feng G Y, Dai S Y, Wang S T, Li G, Zhang H and Zhou S H. 2017. Femtosecond pulsed laser ablation in microfluidics for synthesis of photoluminescent ZnSe quantum dots. *Appl. Surf. Sci.* **414**, 205–211.
[69] Streubel R, Bendt G and Gökce B. 2016. Pilot-scale synthesis of metal nanoparticles by high-speed pulsed laser ablation in liquids. *Nanotechnology* **27**, 205602.
[70] Amans D, Diouf M, Lam J, Ledoux G and Dujardin C. 2017. Origin of the nano-carbon allotropes in pulsed laser ablation in liquids synthesis. *J. Colloid Interface Sci.* **489**, 114–125.
[71] Wazeer A, Das A, Sinha A and Karmakar A. 2023. Nanomaterials synthesis via laser ablation in liquid: a review. *J. Inst. Eng. India Ser. D* **104**, 413–426.
[72] Khairani I Y, Mínguez-Vega G, Doñate-Buendía C and Gökce B. 2023. Green nanoparticle synthesis at scale: a perspective on overcoming the limits of pulsed laser ablation in liquids for high-throughput production. *Phys. Chem. Chem. Phys.* **25**, 19380–19408.
[73] Thanh N T K, Maclean N and Mahiddine S. 2014. Mechanisms of nucleation and growth of nanoparticles in solution. *Chem. Rev.* **114**, 7610–7630.
[74] Moura C G, Pereira R S F, Andritschky M, Lopes A L B, de Freitas Grilo J P, Do Nascimento R M and Silva F S. 2017. Effects of laser fluence and liquid media on preparation of small Ag nanoparticles by laser ablation in liquid. *Opt. Laser Technol.* **97**, 20–28.
[75] Subhan A, Mourad A H I and Al-Douri Y. 2022. Influence of laser process parameters, liquid medium, and external field on the synthesis of colloidal metal nanoparticles using pulsed laser ablation in liquid: a review. *Nanomaterials* **12**, 2144.
[76] Perez-Lopez C A, Perez-Taborda J A, Riascos H and Avila A. 2020. The influence of pulsed laser ablation in liquids parameters on the synthesis of ZnO nanoparticles. *J. Phys.: Conf. Ser.* **1541**, 012019.

[77] Dittrich S, Barcikowski S and Gökce B. 2021. Plasma and nanoparticle shielding during pulsed laser ablation in liquids cause ablation efficiency decrease. *Opto-Electron. Adv.* **4**, 200072.
[78] Yousif N A and Al-Jawad S M H. 2021. Influence of laser wavelength on morphological and optical properties of ZnO nanoparticles prepared by laser ablation in water. *J. Phys.: Conf. Ser.* **1795**, 012056.
[79] Balachandran A, Sreenilayam S P, Madanan K, Thomas S and Brabazon D. 2022. Nanoparticle production via laser ablation synthesis in solution method and printed electronic application—a brief review. *Results Eng.* **16**, 100646.
[80] Kalus M R, Lanyumba R, Barcikowski S and Gökce B. 2021. Discrimination of ablation, shielding, and interface layer effects on the steady-state formation of persistent bubbles under liquid flow conditions during laser synthesis of colloids. *J. Flow Chem.* **11**, 773–792.
[81] Park Y E, Shin S K and Park S M. 2013. The physical effects on the formation of polyynes by laser ablation. *Chem. Phys. Lett.* **568-569**, 112–116.
[82] Inoue K, Matsutani R, Sanada T and Kojima K. 2010. Preparation of long-chain polyynes of $C_{24}H_2$ and $C_{26}H_2$ by liquid-phase laser ablation in decalin. *Carbon* **48**, 4209–4211.
[83] Marzun G, Bönnemann H, Lehmann C, Spliethoff B, Weidenthaler C and Barcikowski S. 2017. Role of dissolved and molecular oxygen on Cu and PtCu alloy particle structure during laser ablation synthesis in liquids. *ChemPhysChem* **18**, 1175–1184.
[84] Wagener P, Jakobi J, Rehbock C, Chakravadhanula V S K, Thede C, Wiedwald U, Bartsch M, Kienle L and Barcikowski S. 2016. Solvent-surface interactions control the phase structure in laser-generated iron-gold core-shell nanoparticles. *Sci. Rep.* **6**, 23352.
[85] Jendrzej S, Gökce B, Epple M and Barcikowski S. 2017. How size determines the value of gold: economic aspects of wet chemical and laser-based metal colloid synthesis. *ChemPhysChem* **18**, 1012–1019.
[86] Marchand P, Makwana N M, Tighe C J, Gruar R I, Parkin I P, Carmalt C J and Darr J A. 2016. High-throughput synthesis, screening, and scale-up of optimized conducting indium tin oxides. *ACS Comb Sci.* **18**, 130–137.
[87] Gruar R I, Tighe C J and Darr J A. 2013. Scaling-up a confined jet reactor for the continuous hydrothermal manufacture of nanomaterials. *Ind. Eng. Chem. Res.* **52**, 5270–5281.
[88] Tighe C J, Cabrera R Q, Gruar R I and Darr J A. 2013. Scale up production of nanoparticles: continuous supercritical water synthesis of Ce–Zn oxides. *Ind. Eng. Chem. Res.* **52**, 5522–5528.
[89] Mueller R, Mädler L and Pratsinis S E. 2003. Nanoparticle synthesis at high production rates by flame spray pyrolysis. *Chem. Eng. Sci.* **58**, 1969–1976.
[90] Gerken L R H, Neuer A L, Gschwend P M, Keevend K, Gogos A, Anthis A H C, Aengenheister L, Pratsinis S E, Plasswilm L and Herrmann I K. 2021. Scalable synthesis of ultrasmall metal oxide radio-enhancers outperforming gold. *Chem. Mater.* **33**, 3098–3112.
[91] Zhang H Q, Zou G S, Liu L, Tong H, Li Y, Bai H L and Wu A P. 2017. Synthesis of silver nanoparticles using large-area arc discharge and its application in electronic packaging. *J. Mater. Sci.* **52**, 3375–3387.
[92] Kalus M R, Bärsch N, Streubel R, Gökce E, Barcikowski S and Gökce B. 2017. How persistent microbubbles shield nanoparticle productivity in laser synthesis of colloids—quantification of their volume, dwell dynamics, and gas composition. *Phys. Chem. Chem. Phys.* **19**, 7112–7123.
[93] Friedenauer T, Buck K, Eberwein M, Bünte A L, Rehbock C and Barcikowski S. 2023. Efficient synthesis of submicrometer-sized active pharmaceuticals by laser fragmentation in a liquid-jet passage reactor with minimum degradation. *Part. Part. Syst. Charact.* **40**, 2300034.
[94] Tack M, Usama M, Kazamer N, Exner K S, Brodmann M, Barcikowski S and Reichenberger S. 2024. Continuous and scalable laser synthesis of atom clusters with tunable surface oxidation for electrocatalytic water splitting. *ACS Appl. Energy Mater* **7**, 4057–4067.
[95] Al-Antaki A H M, Luo X, Duan X F, Lamb R N, Hutchison W D, Lawrance W and Raston C L. 2019. Continuous flow copper laser ablation synthesis of copper(I and II) oxide nanoparticles in water. *ACS Omega* **4**, 13577–13584.
[96] Khairani I Y, Spellauge M, Riahi F, Huber H P, Gökce B and Doñate-Buendía C. 2024. Parallel diffractive multi-beam pulsed-laser ablation in liquids toward cost-effective gram per hour nanoparticle productivity. *Adv. Photonics Res.* **5**, 2300290.
[97] Streubel R, Barcikowski S and Gökce B. 2016. Continuous multigram nanoparticle synthesis by high-power, high-repetition-rate ultrafast laser ablation in liquids. *Opt. Lett.* **41**, 1486–1489.
[98] Zhang D S, Gökce B and Barcikowski S. 2017. Laser synthesis and processing of colloids: fundamentals and applications. *Chem. Rev.* **117**, 3990–4103.
[99] Waag F et al. 2017. Adjusting the catalytic properties of cobalt ferrite nanoparticles by pulsed laser fragmentation in water with defined energy dose. *Sci. Rep.* **7**, 13161.
[100] Zhang D S, Lau M, Lu S W, Barcikowski S and Gökce B. 2017. Germanium sub-microspheres synthesized by picosecond pulsed laser melting in liquids: educt size effects. *Sci. Rep.* **7**, 40355.
[101] Lau M and Barcikowski S. 2015. Quantification of mass-specific laser energy input converted into particle properties during picosecond pulsed laser fragmentation of zinc oxide and boron carbide in liquids. *Appl. Surf. Sci.* **348**, 22–29.
[102] Nyabadza A, Vázquez M and Brabazon D. 2022. Magnesium nanoparticle synthesis from powders via LASIS—effects of liquid medium, laser pulse width and ageing on nanoparticle size, concentration, stability and electrical properties. *Colloids Surf. A* **651**, 129651.
[103] Ziefuß A R, Barcikowski S and Rehbock C. 2019. Synergism between specific halide anions and pH effects during nanosecond laser fragmentation of ligand-free gold nanoparticles. *Langmuir* **35**, 6630–6639.
[104] González-Rubio G, Guerrero-Martínez A and Liz-Marzán L M. 2016. Reshaping, fragmentation, and assembly of gold nanoparticles assisted by pulse lasers. *Acc. Chem. Res.* **49**, 678–686.
[105] Ishikawa Y, Feng Q and Koshizaki N. 2010. Growth fusion of submicron spherical boron carbide particles by repetitive pulsed laser irradiation in liquid media. *Appl. Phys. A* **99**, 797–803.
[106] Wang H Q, Pyatenko A, Kawaguchi K, Li X Y, Swiatkowska-Warkocka Z and Koshizaki N. 2010. Selective pulsed heating for the synthesis of semiconductor and metal submicrometer spheres. *Angew. Chem., Int. Ed.* **49**, 6361–6364.
[107] Rehbock C, Zwartscholten J and Barcikowski S. 2014. Biocompatible gold submicrometer spheres with variable surface texture fabricated by pulsed laser melting in liquid. *Chem. Lett.* **43**, 1502–1504.
[108] Ishikawa Y, Shimizu Y, Sasaki T and Koshizaki N. 2007. Boron carbide spherical particles encapsulated in graphite prepared by pulsed laser irradiation of boron in liquid medium. *Appl. Phys. Lett.* **91**, 161110.
[109] Li L, Zhang J Y, Wang Y Y, Zaman F U, Zhang Y M, Hou L R and Yuan C Z. 2021. Laser irradiation construction of nanomaterials toward electrochemical energy storage and conversion: ongoing progresses and challenges. *InfoMat* **3**, 1393–1421.

[110] Wang H Q, Miyauchi M, Ishikawa Y, Pyatenko A, Koshizaki N, Li Y, Li L, Li X Y, Bando Y and Golberg D. 2011. Single-crystalline rutile TiO_2 hollow spheres: room-temperature synthesis, tailored visible-light-extinction, and effective scattering layer for quantum dot-sensitized solar cells. *J. Am. Chem. Soc.* **133**, 19102–19109.

[111] Ishikawa Y, Koshizaki N, Pyatenko A, Saitoh N, Yoshizawa N and Shimizu Y. 2016. Nano- and submicrometer-sized spherical particle fabrication using a submicroscopic droplet formed using selective laser heating. *J. Phys. Chem. C* **120**, 2439–2446.

[112] Song X Y, Qiu Z W, Yang X P, Gong H B, Zheng S H, Cao B Q, Wang H, Möhwald H and Shchukin D. 2014. Submicron-lubricant based on crystallized Fe_3O_4 spheres for enhanced tribology performance. *Chem. Mater.* **26**, 5113–5119.

[113] Tiedemann D, Taylor U, Rehbock C, Jakobi J, Klein S, Kues W A, Barcikowski S and Rath D. 2014. Reprotoxicity of gold, silver, and gold–silver alloy nanoparticles on mammalian gametes. *Analyst* **139**, 931–942.

[114] Salim E T, Saimon J A, Muhsin M S, Fakhri M A, Amin M H, Azzahrani A S and Ibrahim R K. 2024. Mesoporous Ag@WO_3 core–shell, an investigation at different concentrated environment employing laser ablation in liquid. *Sci. Rep.* **14**, 5473.

[115] Lin F, Yang J, Lu S H, Niu K Y, Liu Y, Sun J and Du X W. 2010. Laser synthesis of gold/oxide nanocomposites. *J. Mater. Chem.* **20**, 1103–1106.

[116] D'Urso L, Spadaro S, Bonsignore M, Santangelo S, Compagnini G, Neri F, Fazio E, Torrisi L and Cutroneo M. 2018. Zinc oxide nanocolloids prepared by picosecond pulsed laser ablation in water at different temperatures. *EPJ Web Conf.* **167**, 04008.

[117] Hu S, Goenaga G, Melton C, Zawodzinski T A and Mukherjee D. 2016. PtCo/CoO_x nanocomposites: bifunctional electrocatalysts for oxygen reduction and evolution reactions synthesized via tandem laser ablation synthesis in solution-galvanic replacement reactions. *Appl. Catal. B* **182**, 286–296.

[118] Yan Z J, Bao R Q and Chrisey D B. 2011. Generation of Ag_2O micro-/nanostructures by pulsed excimer laser ablation of Ag in aqueous solutions of polysorbate 80. *Langmuir* **27**, 851–855.

[119] Amendola V, Scaramuzza S, Carraro F and Cattaruzza E. 2017. Formation of alloy nanoparticles by laser ablation of Au/Fe multilayer films in liquid environment. *J. Colloid Interface Sci.* **489**, 18–27.

[120] Altowyan A S, Mostafa A M and Ahmed H A. 2021. Effect of liquid media and laser energy on the preparation of Ag nanoparticles and their nanocomposites with Au nanoparticles via laser ablation for optoelectronic applications. *Optik* **241**, 167217.

[121] Waag F, Li Y, Ziefuß A R, Bertin E, Kamp M, Duppel V, Marzun G, Kienle L, Barcikowski S and Gökce B. 2019. Kinetically-controlled laser-synthesis of colloidal high-entropy alloy nanoparticles. *RSC Adv.* **9**, 18547–18558.

[122] Johny J et al. 2022. Laser-generated high entropy metallic glass nanoparticles as bifunctional electrocatalysts. *Nano Res.* **15**, 4807–4819.

[123] Mafuné F, Kohno J Y, Takeda Y, Kondow T and Sawabe H. 2000. Formation and size control of silver nanoparticles by laser ablation in aqueous solution. *J. Phys. Chem. B* **104**, 9111–9117.

[124] De Bonis A, Galasso A, Santagata A and Teghil R. 2016. Laser ablation of GaAs in liquid: the role of laser pulse duration. *J. Phys. D: Appl. Phys.* **49**, 035301.

[125] Mori K, Hashimoto N, Kamiuchi N, Yoshida H, Kobayashi H and Yamashita H. 2021. Hydrogen spillover-driven synthesis of high-entropy alloy nanoparticles as a robust catalyst for CO_2 hydrogenation. *Nat. Commun.* **12**, 3884.

[126] Sun Y F and Dai S. 2021. High-entropy materials for catalysis: a new frontier. *Sci. Adv.* **7**, eabg1600.

[127] Amiri A and Shahbazian-Yassar R. 2021. Recent progress of high-entropy materials for energy storage and conversion. *J. Mater. Chem. A* **9**, 782–823.

[128] He K, Wang C, He Y L, Su J T and Chen X D. 2023. Artificial neuron devices. *Chem. Rev.* **123**, 13796–13865.

[129] Kim J, Kwon S M, Kang Y K, Kim Y H, Lee M J, Han K, Facchetti A, Kim M G and Park S K. 2019. A skin-like two-dimensionally pixelized full-color quantum dot photodetector. *Sci. Adv.* **5**, eaax8801.

[130] Hu Y M et al. 2023. Perovskite-based photodetector for real-time and quantitative monitoring of sports motion. *iScience* **26**, 108298.

[131] Guo J X et al. 2024. Type-printable photodetector arrays for multichannel meta-infrared imaging. *Nat. Commun.* **15**, 5193.

[132] Cho H, Lee I, Jang J, Kim J H, Lee H, Park S and Wang G. 2023. Real-time finger motion recognition using skin-conformable electronics. *Nat. Electron.* **6**, 619–629.

[133] Chen Z C, Liu H J, Chang Y C, Chen B J and Chang S J. 2023. Ag-nanoparticle-coupled UV-responsive gelatin nanofiber photodetectors. *ACS Appl. Nano Mater.* **6**, 9298–9305.

[134] Sun X L, Sun J M, Xu J L, Li Z Q, Li R, Yang Z X, Ren F, Jia Y C and Chen F. 2021. A plasmon-enhanced $SnSe_2$ photodetector by non-contact Ag nanoparticles. *Small* **17**, 2102351.

[135] Montaño-Priede J L, Sanromán-Iglesias M, Zabala N, Grzelczak M and Aizpurua J. 2023. Robust rules for optimal colorimetric sensing based on gold nanoparticle aggregation. *ACS Sens.* **8**, 1827–1834.

[136] Lee J W, Kim D Y, Baek S, Yu H and So F. 2016. Inorganic UV–visible–SWIR broadband photodetector based on monodisperse PbS nanocrystals. *Small* **12**, 1328–1333.

[137] Ghods S, Esfandiar A, Choi J H, Iraji Zad A, Josline M J, Kim S and Lee J H. 2023. Gapless linear dispersion in Bi_2Se_3 nanoparticles for high-performance broadband photodetectors. *Mater. Today Phys.* **38**, 101235.

[138] Gao Z Y, Chen S, Li R, Lou Z, Han W, Jiang K, Qu F Y and Shen G Z. 2021. An artificial olfactory system with sensing, memory and self-protection capabilities. *Nano Energy* **86**, 106078.

[139] Wang L, Li W H, Wan L J and Wen D Z. 2023. An artificial olfactory system based on a memristor can simulate organ injury and functions in air purification. *ACS Sens.* **8**, 4810–4817.

[140] Lee S W, Kang M G, Han J K, Yun S Y, Park I and Choi Y K. 2023. An artificial olfactory sensory neuron for selective gas detection with in-sensor computing. *Device* **1**, 100063.

[141] Shinmyo N, Iwata T, Hashizume K, Kuroki K and Sawada K 2017. Development of potentiometric miniature gas sensor arrays feasible for small olfactory chips and gas recognition from their response patterns. *In 2017 IEEE SENSORS* (IEEE) pp 1–3

[142] Abideen Z U et al. 2023. Oxygen vacancies engineering in thick semiconductor films via deep ultraviolet photoactivation for selective and sensitive gas sensing. *Adv. Electron. Mater.* **9**, 2200905.

[143] Abideen Z U, Choi J G, Yuwono J A, Lee W J, Murugappan K, Kumar P V, Nisbet D R, Trần-Phú T, Yoon M H and Tricoli A. 2023. Structural engineering three-dimensional nano-heterojunction networks for high-performance photochemical sensing. *ACS Appl. Mater. Interfaces* **15**, 56464–56477.

[144] Cho I et al. 2023. Deep-learning-based gas identification by time-variant illumination of a single micro-LED-embedded gas sensor. *Light Sci. Appl.* **12**, 95.

[145] Lee J, Jung Y, Sung S H, Lee G, Kim J, Seong J, Shim Y S, Chan Jun S and Jeon S. 2021. High-performance gas sensor

array for indoor air quality monitoring: the role of Au nanoparticles on WO_3, SnO_2, and NiO-based gas sensors. *J. Mater. Chem. A* **9**, 1159–1167.
[146] Urs K M B, Katiyar N K, Kumar R, Biswas K, Singh A K, Tiwary C S and Kamble V. 2020. Multi-component (Ag–Au–Cu–Pd–Pt) alloy nanoparticle-decorated p-type 2D-molybdenum disulfide (MoS_2) for enhanced hydrogen sensing. *Nanoscale* **12**, 11830–11841.
[147] Yeom J, Choe A, Lim S, Lee Y, Na S and Ko H. 2020. Soft and ion-conducting hydrogel artificial tongue for astringency perception. *Sci. Adv.* **6**, eaba5785.
[148] Wu X and Toko K. 2023. Taste sensor with multiarray lipid/-polymer membranes. *Trends Anal. Chem.* **158**, 116874.
[149] Hwang C, Song Y, Baek S, Choi J G and Park S. 2024. Dual-biased metal oxide electrolyte-gated thin-film transistors for enhanced protonation in complex biofluids. *Sci. Rep.* **14**, 30772.
[150] Kang D H, Choi J G, Lee W J, Heo D, Wang S, Park S and Yoon M H. 2023. Aqueous electrolyte-gated solution-processed metal oxide transistors for direct cellular interfaces. *APL Bioeng.* **7**, 026102.
[151] Ye J, Fan M Z, Zhang X Y, Liang Q, Zhang Y S, Zhao X Y, Lin C T and Zhang D M. 2024. A novel biomimetic electrochemical taste-biosensor based on conformational changes of the taste receptor. *Biosens. Bioelectron.* **249**, 116001.
[152] Chen A J, Wang R L, Kang Y Y, Liu J, Wu J R, Zhang Y L, Zhang Y L and Shao L Q. 2023. Tongue−brain-transported ZnO nanoparticles induce abnormal taste perception. *Adv. Healthcare Mater.* **12**, 2203316.
[153] Kumar S, Bhondekar A P, Jain P, Bagchi S, Sharma A, Kumar R and Mishra S. 2018. Artificial lipid membrane: surface modification and effect in taste sensing. *IOP Conf. Ser.: Mater. Sci. Eng.* **360**, 012039.
[154] Hensel R C, Braunger M L, Oliveira B, Shimizu F M, Oliveira O N Jr, Hillenkamp M, Riul A Jr and Rodrigues V. 2021. Controlled incorporation of silver nanoparticles into layer-by-layer polymer films for reusable electronic tongues. *ACS Appl. Nano Mater.* **4**, 14231–14240.
[155] Do H H, Cho J H, Han S M, Ahn S H and Kim S Y. 2021. Metal–organic-framework- and MXene-based taste sensors and glucose detection. *Sensors* **21**, 7423.
[156] Shin J H, Lee M J, Choi J H, Song J A, Kim T H and Oh B K. 2020. Electrochemical H_2O_2 biosensor based on horseradish peroxidase encapsulated protein nanoparticles with reduced graphene oxide-modified gold electrode. *Nano Converg.* **7**, 39.
[157] Zhai D Y, Liu B R, Shi Y, Pan L J, Wang Y Q, Li W B, Zhang R and Yu G H. 2013. Highly sensitive glucose sensor based on Pt nanoparticle/polyaniline hydrogel heterostructures. *ACS Nano* **7**, 3540–3546.
[158] Alencar L M, Silva A W B N, Trindade M A G, Salvatierra R V, Martins C A and Souza V H R. 2022. One-step synthesis of crumpled graphene fully decorated by copper-based nanoparticles: application in H_2O_2 sensing. *Sens. Actuators B* **360**, 131649.
[159] Vinoth S and Wang S F. 2024. Interspersed of scheelite-type $BaWO_4$ nanoparticles decorated on CNF for the electrocatalytic sensing of theobromine in food products. *ACS Appl. Nano Mater.* **7**, 25388–25399.
[160] Chen Z T, Zhang Q Q, Shan J Z, Lu Y L and Liu Q J. 2020. Detection of bitter taste molecules based on odorant-binding protein-modified screen-printed electrodes. *ACS Omega* **5**, 27536–27545.
[161] Saraf N, Barkam S, Peppler M, Metke A, Vázquez-Guardado A, Singh S, Emile C, Bico A, Rodas C and Seal S. 2019. Microsensor for limonin detection: an indicator of citrus greening disease. *Sens. Actuators B* **283**, 724–730.
[162] Jia J J, Zhang S Y, Ma L, Zheng L, Yu S B, Shen C H, Fu H Y, Wang S T and She Y B. 2022. Colorimetric sensor arrays for the differentiation of baijiu based on amino-acid-modified gold nanoparticles. *Sci. Rep.* **12**, 18596.
[163] Yu Y Y et al. 2023. Bimetallic bionic taste sensor for perception of the synergistic effect of umami substances. *Biosens. Bioelectron.* **234**, 115357.
[164] Wang J F, Suo J, Liu D D, Zhao Y L, Tian Y L, Bryanston-Cross P, Li W J and Wang Z B. 2024. A nanoparticle-based artificial ear for personalized classification of emotions in the human voice using deep learning. *ACS Appl. Mater. Interfaces* **16**, 51274–51282.
[165] Gao Y, Song J F, Li S M, Elowsky C, Zhou Y, Ducharme S, Chen Y M, Zhou Q and Tan L. 2016. Hydrogel microphones for stealthy underwater listening. *Nat. Commun.* **7**, 12316.
[166] Lattanzi E and Freschi V. 2020. Evaluation of human standing balance using wearable inertial sensors: a machine learning approach. *Eng. Appl. Artif. Intell.* **94**, 103812.
[167] Yun S Y, Han J K, Lee S W, Yu J M, Jeon S B and Choi Y K. 2023. Self-aware artificial auditory neuron with a triboelectric sensor for spike-based neuromorphic hardware. *Nano Energy* **109**, 108322.
[168] Liu Y Q, Li E L, Wang X M, Chen Q Z, Zhou Y L, Hu Y Y, Chen G X, Chen H P and Guo T L. 2020. Self-powered artificial auditory pathway for intelligent neuromorphic computing and sound detection. *Nano Energy* **78**, 105403.
[169] Lenk C et al. 2023. Neuromorphic acoustic sensing using an adaptive microelectromechanical cochlea with integrated feedback. *Nat. Electron.* **6**, 370–380.
[170] Jiang Y, Zhang Y F, Ning C, Ji Q Q, Peng X, Dong K and Wang Z L. 2022. Ultrathin eardrum-inspired self-powered acoustic sensor for vocal synchronization recognition with the assistance of machine learning. *Small* **18**, 2106960.
[171] Lang C H, Fang J, Shao H, Ding X and Lin T. 2016. High-sensitivity acoustic sensors from nanofibre webs. *Nat. Commun.* **7**, 11108.
[172] Park J et al. 2022. Frequency-selective acoustic and haptic smart skin for dual-mode dynamic/static human-machine interface. *Sci. Adv.* **8**, eabj9220.
[173] Lin Z W, Duan S S, Liu M Y, Dang C, Qian S T, Zhang L X, Wang H L, Yan W and Zhu M F. 2024. Insights into materials, physics, and applications in flexible and wearable acoustic sensing technology. *Adv. Mater.* **36**, 2306880.
[174] Gou G Y et al. 2022. Two-stage amplification of an ultrasensitive MXene-based intelligent artificial eardrum. *Sci. Adv.* **8**, eabn2156.
[175] Lee S, Kim J, Yun I, Bae G Y, Kim D, Park S, Yi I M, Moon W, Chung Y and Cho K. 2019. An ultrathin conformable vibration-responsive electronic skin for quantitative vocal recognition. *Nat. Commun.* **10**, 2468.
[176] Xu H C et al. 2021. Stretchable and anti-impact iontronic pressure sensor with an ultrabroad linear range for biophysical monitoring and deep learning-aided knee rehabilitation. *Microsyst. Nanoeng.* **7**, 92.
[177] Yan W et al. 2022. Single fibre enables acoustic fabrics via nanometre-scale vibrations. *Nature* **603**, 616–623.
[178] Lin Z W et al. 2022. A personalized acoustic interface for wearable human–machine interaction. *Adv. Funct. Mater.* **32**, 2109430.
[179] Hazan Y, Levi A, Nagli M and Rosenthal A. 2022. Silicon-photonics acoustic detector for optoacoustic microtomography. *Nat. Commun.* **13**, 1488.
[180] Zhao Y C, Gao S H, Zhang X, Huo W X, Xu H, Chen C, Li J, Xu K X and Huang X. 2020. Fully flexible electromagnetic vibration sensors with annular field confinement origami magnetic membranes. *Adv. Funct. Mater.* **30**, 2001553.
[181] Tao L Q et al. 2017. An intelligent artificial throat with sound-sensing ability based on laser induced graphene. *Nat. Commun.* **8**, 14579.
[182] Xiang Z Y, Li L H, Lu Z H, Yu X X, Cao Y W, Tahir M, Yao Z Y and Song Y L. 2023. High-performance

microcone-array flexible piezoelectric acoustic sensor based on multicomponent lead-free perovskite rods. *Matter* **6**, 554–569.
[183] Yi L Z, Jiao W H, Wu K, Qian L H, Yu X X, Xia Q, Mao K M, Yuan S L, Wang S and Jiang Y T. 2015. Nanoparticle monolayer-based flexible strain gauge with ultrafast dynamic response for acoustic vibration detection. *Nano Res.* **8**, 2978–2987.
[184] Huang P C, Chaney E J, Shelton R L and Boppart S A. 2018. Magnetomotive displacement of the tympanic membrane using magnetic nanoparticles: toward enhancement of sound perception. *IEEE Trans. Biomed. Eng.* **65**, 2837–2846.
[185] Andò B, Baglio S, Lombardo C O, Marletta V and Pistorio A. 2016. A low-cost accelerometer developed by inkjet printing technology. *IEEE Trans. Instrum. Meas.* **65**, 1242–1248.
[186] Liu G D, Yang W D, Wang C H and Rao J Y. 2021. A rapid fabrication approach for the capacitive accelerometer based on 3D printing and a silver particle-free ink. *J. Mater. Sci., Mater. Electron.* **32**, 17901–17910.
[187] Fernández-Valdés D, Torres-Torres C, Martínez-González C L, Trejo-Valdez M, Hernández-Gómez L H and Torres-Martínez R. 2016. Gyroscopic behavior exhibited by the optical Kerr effect in bimetallic Au–Pt nanoparticles suspended in ethanol. *J. Nanopart. Res.* **18**, 204.
[188] Zhang H J and Yin Z Q. 2023. Highly sensitive gyroscope based on a levitated nanodiamond. *Opt. Express* **31**, 8139–8151.
[189] Krug B and Asumadu J 2016. Magnetic nanoparticle-based gyroscopic detection device: a review. *In 2016 IEEE International Conference on Industrial Technology (ICIT)* (IEEE) pp 658–662
[190] Tang J, Guo H, An P, Chen M, Tsoukalas D, Shi Y B, Liu J, Xue C Y and Zhang W D. 2014. ZnO nanoparticles embedded in polyethylene-glycol (PEG) matrix as sensitive strain gauge elements. *J. Nanopart. Res.* **16**, 2714.
[191] Shengbo S, Lihua L, Aoqun J, Qianqian D, Jianlong J, Qiang Z and Wendong Z. 2018. Highly sensitive wearable strain sensor based on silver nanowires and nanoparticles. *Nanotechnology* **29**, 255202.
[192] Yang Y N, Shi L J, Cao Z R, Wang R R and Sun J. 2019. Strain sensors with a high sensitivity and a wide sensing range based on a $Ti_3C_2T_X$ (MXene) nanoparticle–nanosheet hybrid network. *Adv. Funct. Mater.* **29**, 1807882.
[193] Neella N, Gaddam V, Nayak M M, Dinesh N S and Rajanna K. 2017. Scalable fabrication of highly sensitive flexible temperature sensors based on silver nanoparticles coated reduced graphene oxide nanocomposite thin films. *Sens. Actuators A* **268**, 173–182.
[194] Al-Hayali S K, Salman A M and Al-Janabi A H. 2021. High sensitivity balloon-like interferometric optical fiber humidity sensor based on tuning gold nanoparticles coating thickness. *Measurement* **170**, 108703.
[195] Kim H et al. 2018. Transparent, flexible, conformal capacitive pressure sensors with nanoparticles. *Small* **14**, 1703432.
[196] Yu Z et al. 2020. Stretchable tactile sensor with high sensitivity and dynamic stability based on vertically aligned urchin-shaped nanoparticles. *Mater. Today Phys.* **14**, 100219.
[197] Yoo J Y, Seo M H, Lee J S, Choi K W, Jo M S and Yoon J B. 2018. Industrial grade, bending-insensitive, transparent nanoforce touch sensor via enhanced percolation effect in a hierarchical nanocomposite film. *Adv. Funct. Mater.* **28**, 1804721.
[198] Chen M R et al. 2019. An ultrahigh resolution pressure sensor based on percolative metal nanoparticle arrays. *Nat. Commun.* **10**, 4024.
[199] Segev-Bar M, Landman A, Nir-Shapira M, Shuster G and Haick H. 2013. Tunable touch sensor and combined sensing platform: toward nanoparticle-based electronic skin. *ACS Appl. Mater. Interfaces* **5**, 5531–5541.
[200] Herrmann J, Müller K H, Reda T, Baxter G R, Raguse B, de Groot G J J B, Chai R, Roberts M and Wieczorek L. 2007. Nanoparticle films as sensitive strain gauges. *Appl. Phys. Lett.* **91**, 183105.
[201] Sangeetha N M, Decorde N, Viallet B, Viau G and Ressier L. 2013. Nanoparticle-based strain gauges fabricated by convective self assembly: strain sensitivity and hysteresis with respect to nanoparticle sizes. *J. Phys. Chem. C* **117**, 1935–1940.
[202] Ketelsen B, Schlicke H, Schulze V R, Bittinger S C, Wu S D, Hsu S H and Vossmeyer T. 2023. Nanoparticle-based strain gauges: anisotropic response characteristics, multidirectional strain sensing, and novel approaches to healthcare applications. *Adv. Funct. Mater.* **33**, 2210065.
[203] Jheng W W, Su Y S, Hsieh Y L, Lin Y J, Tzeng S D, Chang C W, Song J M and Kuo W. 2021. Gold nanoparticle thin film-based strain sensors for monitoring human pulse. *ACS Appl. Nano Mater.* **4**, 1712–1718.
[204] Lee J, Kim S, Lee J, Yang D, Park B C, Ryu S and Park I. 2014. A stretchable strain sensor based on a metal nanoparticle thin film for human motion detection. *Nanoscale* **6**, 11932–11939.
[205] Zhang X J, Zhang Y C, Zhang W L, Dai Y and Xia F. 2021. Gold nanoparticles-deranged double network for Janus adhesive-tough hydrogel as strain sensor. *Chem. Eng. J.* **420**, 130447.
[206] Choe A, Yeom J, Shanker R, Kim M P, Kang S and Ko H. 2018. Stretchable and wearable colorimetric patches based on thermoresponsive plasmonic microgels embedded in a hydrogel film. *NPG Asia Mater.* **10**, 912–922.
[207] Maji S, Cesur B, Zhang Z Y, De Geest B G and Hoogenboom R. 2016. Poly(n-isopropylacrylamide) coated gold nanoparticles as colourimetric temperature and salt sensors. *Polym. Chem.* **7**, 1705–1710.
[208] Liu Y D, Han X G, He L and Yin Y D. 2012. Thermoresponsive assembly of charged gold nanoparticles and their reversible tuning of plasmon coupling. *Angew. Chem., Int. Ed.* **51**, 6373–6377.
[209] Kano S and Mekaru H. 2020. Nonporous inorganic nanoparticle-based humidity sensor: evaluation of humidity hysteresis and response time. *Sensors* **20**, 3858.
[210] Yadav N, Chaudhary P, Dey K K, Yadav S, Yadav B C and Yadav R R. 2020. Non-functionalized Au nanoparticles can act as high-performing humidity sensor. *J. Mater. Sci., Mater. Electron.* **31**, 17843–17854.
[211] Guo J H, Liu L, Wang J Y, Zhao X, Zhang Y C and Yan Y. 2024. A diffusive artificial synapse based on charged metal nanoparticles. *Nano Lett.* **24**, 1951–1958.
[212] Zeng Y H, Chu F J, Shih L C, Chen Y C and Chen J S. 2023. Dual light temporal coding modes enabled by nanoparticle-mediated phototransistors via gate bias modulation for brain-inspired visual perception. *ACS Appl. Mater. Interfaces* **15**, 9563–9573.
[213] Sun L, Qu S D and Xu W T. 2023. A retinomorphic neuron for artificial vision and iris accommodation. *Mater. Horiz.* **10**, 5753–5762.
[214] Jiang C P, Liu J Q, Ni Y, Qu S D, Liu L, Li Y, Yang L and Xu W T. 2023. Mammalian-brain-inspired neuromorphic motion-cognition nerve achieves cross-modal perceptual enhancement. *Nat. Commun.* **14**, 1344.
[215] Kim J et al. 2020. Modulation of synaptic plasticity mimicked in Al nanoparticle-embedded IGZO synaptic transistor. *Adv. Electron. Mater.* **6**, 1901072.
[216] Liu P S, Hui F, Aguirre F, Saiz F, Tian L L, Han T T, Zhang Z J, Miranda E and Lanza M. 2022. Nano-memristors with 4 mV switching voltage based on surface-modified copper nanoparticles. *Adv. Mater.* **34**, 2201197.

[217] Wei H, Han H, Guo K, Yu H, Gong J, Ma M, Ni Y, Feng J, Xu Z and Xu W. 2021. Artificial synapses that exploit ionic modulation for perception and integration. *Mater. Today Phys.* **18**, 100329.

[218] Wei H H, Xu Z P, Ni Y, Yang L, Sun L, Gong J D, Zhang S, Qu S D and Xu W T. 2023. Mixed-dimensional nanoparticle–nanowire channels for flexible optoelectronic artificial synapse with enhanced photoelectric response and asymmetric bidirectional plasticity. *Nano Lett.* **23**, 8743–8752.

[219] Wei H H, Ni Y, Sun L, Yu H Y, Gong J D, Du Y, Ma M X, Han H and Xu W T. 2021. Flexible electro-optical neuromorphic transistors with tunable synaptic plasticity and nociceptive behavior. *Nano Energy* **81**, 105648.